Bifurcating flows of plunging airfoils at high Strouhal numbers

D. J. CLEAVER, Z. WANG, and I. GURSUL

Department of Mechanical Engineering, University of Bath, Bath, BA2 7AY, UK.

Force and particle image velocimetry measurements were conducted on a NACA 0012 airfoil undergoing small-amplitude sinusoidal plunge oscillations at low Reynolds numbers and angles of attack in the range 0° to 20°. For angles of attack smaller than and equal to the stall angle, significant bifurcations were observed in the time-averaged lift coefficient at large Strouhal numbers. With the frequency gradually increasing very large positive lift coefficients are observed. The velocity measurements showed this to be associated with an upwards deflected jet that is created by the clockwise trailing-edge vortex loitering over the airfoil and pairing with the counter-clockwise vortex to form a vortex dipole with an upwards inclination. Conversely, with the airfoil impulsively started at the maximum frequency and the frequency gradually decreasing, either an upward or downward deflected jet can be created depending upon the starting position and angle of attack. With a downward deflected jet the counter-clockwise vortex loiters instead, giving the vortex dipole a downward inclination. Below the bifurcation frequency, lift force and flow fields are identical for increasing and decreasing frequency. The bifurcation was not observed for very small plunge amplitudes or frequencies due to insufficient trailing-edge vortex strength, nor at larger angles of attack due to greater asymmetry in the strength of the trailing-edge vortices, which creates a preference for a downward deflected jet. Vortex strength and asymmetry parameters are derived from the circulation measurements. It is shown that the most appropriate strength parameter in determining the onset of deflected jets is the circulation normalized by the plunge velocity.

1. Introduction

Birds, insects, and fish use oscillating wings for lift and thrust production. Their astonishing performance and agility have sparked extensive studies of flow physics of oscillating wings. Aspects of unsteady aerodynamics of oscillating airfoils and wings and vortex-dominated flows have been reviewed by Shyy et al. (1999), Triantafyllou *et al.* (2000), Ho *et al.* (2003), and Platzer *et al.* (2008). There is growing interest in biologically inspired flows due to their relevance in the design of Micro Air Vehicles (MAVs) and small unmanned underwater vehicles.

1.1 Lift generation

For MAVs to become a practical reality it will first be necessary to overcome the limitations of the low Reynolds number aerodynamics. In particular the high likelihood of separation and stall at the low Reynolds numbers is typical of micro air vehicles. Natural flyers have managed to circumvent this barrier through the exploitation of unsteady aerodynamic phenomenon, for example the Leading-Edge Vortex (LEV), clap and fling, etc. Of these unsteady aerodynamic phenomenon the LEV is generally accepted (Sane, 2003) as being responsible for the majority of lift augmentation. The LEV is produced during the wing's downstroke and once formed it convects over the upper surface creating a low pressure wave as it passes. The behavior of the LEV once shed will largely be determined by the Strouhal number based on the chord length, which can be considered as the ratio of two time scales:

$$St_c = f c / U_\infty , \qquad (1)$$

where f is the oscillation frequency, c the airfoil chord, and U_∞ the free stream velocity. Hence it is expected that Strouhal number based on the chord length will be important for the unsteady lift.

To produce the LEV, natural flyers use a *large-amplitude low-frequency* flapping motion, hence low St_c, on the order of $O(0.1)$. However, the opposite approach, which is the *small-amplitude high-frequency* (large St_c) motion, has also been considered for MAV applications (Cleaver *et al.*, 2011; 2009a; 2009b). A lift enhancing LEV is still generated by small-amplitude high-frequency motion which is more appropriate for electrical actuators, and also preferable as a stable sensor platform. This approach is also more suitable for exploitation of the aeroelastic vibrations for flow control purposes, through excitation of the frequencies of the dominant inherent instabilities of the separated flows by wing oscillations. It has been shown (Cleaver *et al.*, 2011) that when the excitation frequency corresponds to that of the wake instabilities ($St_c = O(1)$), optimal conditions are reached for lift generation. Fortunately, these frequencies are of the same order of magnitude as the structural frequencies of small vehicles. Hence, it may be advantageous to consider small amplitude high frequency wing motions.

1.2 Thrust generation

Thrust generation with oscillating (plunging, pitching) airfoils or oscillating free stream was discussed nearly hundred years ago. The history of the subject is given in the review article by Platzer *et al.* (2008). At low Strouhal numbers the vortices are spaced symmetrically about the horizontal plane with the clockwise vortex above the counter-clockwise creating a wake similar to a Kármán vortex street, see Figure 1. This is considered drag indicative due to the time-averaged velocity deficit in the wake. With increasing Strouhal number these vortices gradually become inverted creating a reverse Kármán vortex street. (Although it was shown recently that the switch in the vortex array orientation does not exactly coincide with the switch from drag to thrust (Bohl & Koochesfahani, 2009), this picture gives an approximate tool to discuss the state of the flow). Once the reverse Kármán

vortex street is observed, due to the time-averaged velocity surplus in the wake this is generally considered indicative of thrust production. Up to this point, if the airfoil was to be oscillated at zero degrees angle of attack, one would anticipate symmetry about the horizontal plane and therefore zero time-averaged lift.

It has been shown that the most important parameter for thrust generation is the Strouhal number based on the amplitude, which is defined as:

$$St_A = f A / U_\infty , \tag{2}$$

where A is the peak-to-peak amplitude of the trailing-edge. For pure plunging airfoil, this is taken as $A = 2a$, where a is the amplitude of the plunging motion. This parameter can be considered as normalized plunge velocity. It is also related to the maximum effective angle of attack $\alpha_{\text{eff, max}}$,through:

$$\alpha_{eff,\max} = \alpha + \tan^{-1}\frac{U_P}{U_\infty} = \alpha + \tan^{-1}\frac{2\pi f a}{U_\infty} = \alpha + \tan^{-1}\pi St_A \tag{3}$$

where U_P is the maximum plunge velocity. Hence, with increasing St_A, the effective angle of attack increases, and flow separation from the leading-edge and leading-edge vortex formation take place. According to Platzer *et al.* (2008), dynamic stall starts when $St_A \approx 0.11$ for pure plunge oscillations at $\alpha = 0°$ and a Reynolds number $Re=10^6$. For lower Reynolds numbers, separation and stall are expected to start at a lower St_A. The leading-edge vortices are omitted from the flow schematic in Figure 1.

1.3 Deflected jets

For zero mean angle of attack, the symmetry may be broken by deflected jets with increasing Strouhal number. Figure 1 shows the transition towards symmetry breaking. Thus at high enough Strouhal numbers there is the possibility of asymmetric flow fields and non-zero lift even at zero degrees angle of attack. As we will demonstrate, higher time-averaged

lift can be generated in this mode compared to the mean lift produced by the leading-edge vortices. Hence, this is another motivation to investigate *small-amplitude high-frequency* motion.

According to Jones *et al.* (1998) such deflected jets were first observed by Bratt (1950) but not commented on. In their own experiments Jones *et al.* (1998) observed deflected jets when $St_A > 0.32$. The vortex streets could be deflected up or down, hence they were termed *dual* modes. It was also observed that small disturbances could trigger the switch between the modes in a random fashion. Jones *et al.* (1998) was also able to simulate such deflected jets by an inviscid unsteady panel code, however, the jets were very stable and did not exhibit any switch. In the simulations, the direction of the deflection was determined by the sign of the starting vortex when the airfoil starts to move up or down. In viscous simulations, Lewin and Haj-Hariri (2003) observed aperiodic and asymmetric solutions, corresponding to unstable deflected jets for an airfoil oscillating at $St_A \approx 0.48$ and $Re = 500$. Heathcote and Gursul (2007b) experimentally observed jet switching for a NACA 0012 airfoil oscillated in still fluid. The jet switching was observed to be periodic with a period two orders of magnitude larger than the plunging period ($O(100T)$). Recently, von Ellenreider and Pothos (2008) observed stable deflected jets to commence when $St_A > 0.43$ for a NACA 0012 airfoil plunging at $a/c = 0.215$ for $Re = 2{,}700$. The direction, upwards or downwards, was established when the heaving motion is initiated and remains the same as long as the motion is continued. Liang et al. (2011) was able to reproduce the experimental results of Jones et al. (1998) and predicted that the degree of asymmetry increases with Reynolds number in the range of $Re = 252$ to 1,850.

For pitching airfoils, such deflected jets were computationally simulated (Emblemsvag *et al.*, 2002). For a Reynolds number of $Re = 200$, asymmetric flow was predicted for $St_A = 0.42$. Furthermore deflected jets have also been observed experimentally for pitching airfoils

(Godoy-Diana *et al.*, 2008; Godoy-Diana *et al.*, 2009) with onset around $St_A \approx 0.33$ to 0.44 for $Re = 255$. It was also conjectured (Godoy-Diana *et al.*, 2008) that, as natural flyers typically operate in the range $0.2 < St_A < 0.4$, animals using flapping-based propulsion could exploit deflected jets for maneuvering. Indeed, Wang (2000) identified downward deflected vortex dipoles as a possible method of lift generation in hovering insect flight.

Given the potential for large force coefficients, the prediction of the onset conditions for this asymmetry or bifurcation may be very useful for MAV design and control. Emblemsvag *et al.* (2002) was the first to suggest that, at high frequencies, the vortices tend to shed in pairs (vortex dipoles) and this triggers the deflected wakes. Hence, the formation of dipoles is important as the distance between the vortices decrease and strength of the vortices increase with increasing frequency. A symmetry breaking criterion, based on a simple model of a dipole and its self-induced velocity, was suggested by Godoy-Diana *et al.* (2009). The model was developed based on the measured strength of the vortices and the phase velocity of the vortex street for zero mean angle of attack.

1.4 Objectives

Previous studies have focused on the formation of vortex dipoles and deflected jets when the mean angle of attack was zero. These observations led to symmetry breaking and bifurcation at high Strouhal numbers. However, the geometric symmetry is removed when the mean angle of attack is nonzero. Hence a second parameter, which is the angle of attack and defines the degree of *asymmetry*, is introduced in this study. Whether the bifurcations are still observed and, if observed, the range of incidences over which they occur will be investigated by means of flow field and force measurements. It is expected that there will be a competition between the asymmetry due to incidence and the asymmetry introduced by the initial conditions. From a practical point of view, the nonzero mean incidence is more

meaningful. As discussed earlier, lift due to the deflected jets may provide high lift for MAVs in *small-amplitude high-frequency* motion.

To the best of our knowledge no previous study has experimentally measured the effect of deflected jets on the time-averaged force coefficients, nor how the initial conditions determine the direction of the deflected jet. Starting with the stationary airfoil, we measure the time-averaged lift as we increase the frequency very slowly up to a maximum value, and stop the motion. Then we restart the motion impulsively at the maximum frequency and decrease the frequency very slowly. Following this procedure, we identify the bifurcation points for each angle of attack.

The remainder of the paper is as follows. Section 2 explains the experimental set-up, and the methods used for force and velocity measurements. Section 3 presents the bifurcation behavior at different angles of attack using the time-averaged lift measurements and corresponding flow fields. Effects of initial conditions, oscillation amplitude and Reynolds number are investigated. Also, in this section, various bifurcation criteria are developed and discussed.

2. Experimental Methodology

Force and Particle Image Velocimetry (PIV) measurements were conducted on a plunging NACA 0012 airfoil mounted vertically in a closed-loop water tunnel. The airfoil was maintained at a fixed geometric angle of attack with the sinusoidal plunging motion acting normal to the freestream. The vast majority of the experiments presented here are for a Reynolds number based on the chord length of Re = 10,000.

2.1 Experimental setup

The experiments were conducted in a free-surface closed-loop water tunnel (Eidetics Model 1520) at the University of Bath. The water tunnel is capable of flow speeds in the

range 0 to 0.5 m/s and has a working section of dimensions 381 mm x 508 mm x 1530 mm. The turbulence intensity has previously been measured (Heathcote & Gursul, 2007a) by Laser Doppler Velocimetry to be less than 0.5%.

A NACA 0012 airfoil of dimensions 0.1 m chord x 0.3 m span was mounted vertically in a 'shaker' mechanism, see Figure 2. The airfoil was constructed by rapid prototyping from SLS Duraform Prototype PA. The airfoil had two internal 8-mm diameter steel rods spanning from root to tip to ensure a high spanwise stiffness. The tip deformation was monitored with a digital camera and did not exceed 1% of the chord length for the largest amplitude and frequency. The airfoil was placed between an upper and lower end plate with clearances maintained at 2 mm. The oscillations were supplied via a Motavario 0.37 kW three-phase motor, 5:1 wormgear and IMO Jaguar Controller. The position of the root of the airfoil was measured through a rotary encoder attached to the spindle of the worm gear shaft. The rotary encoder was also used to trigger the PIV system.

We consider harmonic plunge oscillations in the form of:

$$h = a \cos 2\pi ft \qquad (4)$$

Normalized amplitude of the plunge oscillations was in the range of a/c = 0.025 to 0.2. The Strouhal number based on the chord length, $St_c = fc/U_\infty$, of the oscillations was varied in the range of St_c = 0 to 3.0, with a maximum uncertainty of ±2.3%. Uncertainties are calculated based on the methods of Moffat (1988) taking into account both bias and precision errors.

2.2 Force measurements

The forces applied in both the streamwise and cross-stream directions were measured via a two-component binocular strain gauge force balance (Frampton *et al.*, 2002). The measured forces include both time-dependent aerodynamic forces and the inertia force in the cross-stream direction. However, as the time-averaged inertial force over a complete cycle is zero,

the time-averaged forces include only the time-averaged aerodynamic component. No attempt was made to estimate the instantaneous aerodynamic forces, as the time-averaged aerodynamic forces are sufficient for the current study.

Three force balances, two aluminium one mild steel, of varying sensitivity (hence flexibility) were used as the oscillation frequency is increased. A fourth very sensitive aluminium force balance was used for the stationary measurements. Within their applicable ranges, the agreement between the three balances was excellent. The signal from the strain gauges was amplified by a Wheatstone bridge circuit and sampled at either 2 kHz for 20,000 samples (stationary cases), or 360 samples per cycle for a minimum of 50 cycles (dynamic cases). To minimize uncertainty the calibration curves consisted of twenty three points, and were performed daily before and after testing. Each data set was repeated a minimum of three times for each force balance.

The uncertainty associated with these time-averaged force measurements increases with increasing frequency. For a typical case the uncertainty of the time-averaged lift coefficient increases from ±0.03 at St_c = 0, to ±0.35 at the maximum Strouhal number. Likewise the uncertainty of the time-averaged drag coefficient increases from ±0.02 to ±0.09 within the same range.

2.3 PIV measurements

A TSI 2D-PIV system consisting of dual 50 mJ Nd:YAG lasers and 8-bit CCD camera of resolution 1600 by 1192 pixels was used to measure the velocity field in the vicinity of the airfoil. The flow was seeded with commercially available hollow glass particles with mean diameter of 4 μm. For measurements over the upper surface of the airfoil, the laser sheet was positioned at mid-span, with the camera located under the tunnel as shown in Fig. 2(a). The shadow created by the airfoil therefore obscured the lower surface. For measurements over

the lower surface the laser sheet was positioned near the side wall of the tunnel as shown in Fig. 2(b). The PIV images were analyzed using the software Insight 3G using a recursive FFT correlator with a final interrogation window size of 16 by 16 pixels to generate a vector field of 199 x 148 vectors. This gave approximately a 1.2 mm (1.2% of the chord length) spatial resolution for the upper surface, and 0.9 mm (0.9% of the chord length) for the lower surface. The estimated uncertainty for velocity measurements is 2% of the freestream velocity U_∞. The time-averaged data is derived from 500 pairs of images, the phase-averaged from 100 pairs for the upper surface, and between 100 and 250 pairs for the lower surface. Where necessary the upper and lower surface data were later merged through interpolation of the upper surface data onto the lower surface grid.

To calculate circulation from the phase-averaged data, the vortex is located using a vortex identification algorithm (Graftieaux *et al.*, 2001; Morgan *et al.*, 2009) with the search centered on the point of maximum absolute vorticity. The radius of the vortex is then determined by continually expanding from the centre, one spatial resolution unit at a time, until the increase in the magnitude of circulation is negative or small (<1%). The circulation calculation itself is done using both line integral and vorticity surface methods (Godoy-Diana *et al.*, 2009). The agreement between the two methods was generally very good. All circulation results presented herein are derived from the average of the two.

3. Results and discussion

3.1 Stationary airfoil

The majority of the experiments for the plunging airfoil were carried out for a Reynolds number of Re = 10,000. As a reference case the lift force measurements for the stationary two-dimensional NACA 0012 airfoil are presented in Figure 3a for three Reynolds numbers, Re = 10,000, 20,000, and 30,000. Also shown are two comparative sets from the literature. The data of Sunada et al. (1997) is for a finite wing at a lower Reynolds number of Re =

4,000. The aspect ratio in this case was AR = 6.75, and it can therefore be considered as a good approximation to the two-dimensional case. Likewise the data of Schluter (2009) is for a finite wing (AR = 5) at Re = 31,000. As the aspect ratio is large, it can also be considered as a good approximation to the two-dimensional case.

Comparing the current data set for Re = 30,000 with that from Schluter at Re = 31,000 one can see reasonable agreement between the two sets. At small angles of attack both curves are nonlinear with the current data consistently lower, perhaps due to freestream turbulence or surface roughness affecting the behaviour of the laminar separation bubble. The curve of Schluter stalls near $\alpha = 9°$, whereas for the current data the stall angle is $\alpha = 10°$. In both cases stall is abrupt suggesting leading edge stall. Comparing the data set for Re = 10,000 with that of Sunada et al. for Re = 4,000 there are very large differences. The lower Reynolds number curve of Sunada et al. is consistently and significantly lower. This is part of a general trend of decreasing lift curve slope with decreasing Reynolds number for $Re < 20{,}000$. Furthermore, the type of stall is very different for $Re < 20{,}000$. The peak is more rounded and the drop less abrupt, suggesting trailing-edge stall. This is in agreement with the flow visualization results of Huang and Lin (1995) for a NACA 0012 airfoil. They showed that for $Re < 20{,}000$ trailing-edge stall commences at angles of attack in the region of 1°, becoming fully stalled once the angle of attack exceeds ~10°. When the Reynolds number is increased, at a critical value the separated laminar flow will trip into turbulence and therefore reattach, forming the laminar separation bubble typical of leading-edge stall. Hence the curves for $Re \geq 20{,}000$ are typical of leading-edge stall, and those for $Re < 20{,}000$ are typical of laminar trailing-edge stall. These are consistent with the time-averaged velocity for $\alpha = 0°$ to 15° shown in Figure 3b for Re = 10,000. Regardless of the type of stall, the location of stall is relatively consistent: $\alpha = 10° \pm 1°$. The angles of attack under consideration in this paper can therefore be classified as: $\alpha = 0°$ and 5° is pre-stall, $\alpha = 10°$ is stall, and $\alpha \geq 12.5°$ is fully

stalled. For the remainder of the paper the Reynolds number will be fixed at Re = 10,000 unless otherwise noted.

3.2 Bifurcations

Shown in Figure 4 is the time-averaged lift coefficient for a NACA 0012 airfoil oscillating at an amplitude of a/c = 0.15, and six different angles of attack. A solid line represents data collected by starting at St_c = 0 (stationary), and then increasing the Strouhal number accumulating data at discrete points along the way. A dashed line represents data collected by impulsively starting at the maximum Strouhal number, and then decreasing the Strouhal number accumulating data at discrete points along the way.

For α = 0° there are three curves. One for increasing frequency, and two for decreasing frequency, where two starting positions of the airfoil are $h_i = +a$ (solid symbol, dashed line) and $h_i = -a$ (open symbol, dashed line). These curves were highly repeatable when the experiments were carried out on different occasions. Up to St_c = 1.5 all three match closely. They all begin at $c_l = 0$ and continue along $c_l = 0$ until $St_c > 1.25$ where all three become slightly positive suggesting a slight asymmetry developing. After St_c = 1.5 the three curves diverge significantly producing two distinct results: increasing and decreasing ($h_i = a$) frequency produce very large positive lift coefficients; decreasing ($h_i = -a$) frequency produces very large negative lift coefficients. Hence for the same experimental conditions two entirely different results are possible; indeed the two results are approximately mirror images of each other in the x-axis. Hereafter where two distinct results exist for the same experimental conditions it shall be termed a dual-flow, with the positive lift coefficient branch termed *mode A* and the negative branch termed *mode B*.

With the angle of attack increased to α = 5° there are similarly two distinct results determined by the initial conditions. Increasing frequency results in mode A, and decreasing

frequency results in mode B. For decreasing frequency the effect of starting position shall be considered in more detail later, but it suffices to say that given a suitable h_i either mode can be produced. For conciseness only a single starting position that produces mode B is considered here, i.e., $h_i = 0$ (moving upwards). Initially both increasing and decreasing frequency demonstrate a gradual increase in lift coefficient with increasing Strouhal number. At around $St_c = 1.5$ the two cases bifurcate, increasing frequency leads to mode A and decreasing frequency leads to mode B. Due to the non-zero angle of attack the two cases are not symmetrical about the x-axis. Mode A results in a maximum lift coefficient of $c_l = 5.3$; and mode B results in a minimum lift coefficient of $c_l = -2.0$.

At an angle of attack of $\alpha = 10°$ there are similar trends. Initially both curves match, gradually increasing until the bifurcation at around $St_c = 1.5$. Again increasing frequency results in mode A and decreasing frequency mode B with the asymmetry further accentuated. The associated maximum and minimum lift coefficients are $c_l = 4.3$ and $c_l = -0.4$ respectively.

At $\alpha = 12.5°$ there are no longer two distinct results at the highest Strouhal number, instead both increasing and decreasing frequency result in a slightly negative lift coefficient. In the low Strouhal number range the match is very close. At $St_c = 1.63$ increasing and decreasing frequency diverge slightly remerging at $St_c = 1.88$. The behavior in this range can be considered as a hysteresis loop. Regardless of hysteresis, both increasing and decreasing frequency result in significant fall from $c_l \approx 2.5$ to $c_l \approx -0.3$.

At $\alpha = 15°$ there is similar behavior to $\alpha = 12.5°$ except the fall in lift does not result in a negative lift coefficient. Again there is small hysteresis between the increasing and decreasing frequency cases around $1.43 < St_c < 1.73$ but it is much reduced in comparison with $\alpha = 12.5°$. The features associated with this post-stall angle of attack and enhanced time-averaged lift were discussed in detail by Cleaver et al. (2009b). The general rise in lift was

associated with the growth of an upper surface leading-edge vortex and its convection along the surface. The peaks were attributed to resonance with the natural wake shedding frequency, its harmonics or subharmonics. The fall in lift at $St_c \approx 1.5$ was attributed to the disintegration of the upper surface LEV (due to a strong vortex-airfoil interaction) combined with the growth of a lower surface LEV.

With the angle of attack increased to $\alpha = 20°$ there is no longer a fall in lift at $St_c \approx 1.5$, instead there is a continued increase in lift coefficient with Strouhal number. Superimposed onto this are several peaks which can be attributed to resonance with the natural wake shedding frequency as for $\alpha = 15°$. The crucial point is that both increasing and decreasing frequency curves match, and there is no hysteresis and bifurcation.

In summary, for angles of attack up to the stall angle, $\alpha \leq 10°$, dual flows are possible resulting in extremely different and potentially very large time-averaged lift coefficients. Which flow field is created is dependent upon the initial conditions. With increasing frequency and $0° < \alpha \leq 10°$ only mode A is achievable. With decreasing frequency, either mode may be obtained depending upon the starting position and angle of attack. In the post-stall region, $10° < \alpha < 20°$, except some minor hysteresis loops, the lift for both increasing and decreasing frequency matches. While the convected leading-edge vortices enhance the time-averaged lift in the post-stall region, there is even higher lift when the bifurcations occur in the pre-stall region. As will be shown below, the mechanism for high lift is deflected (thrust producing) jets at high Strouhal numbers.

3.3 Bifurcation flow fields

Figure 5 and 6 show PIV measurements for $a/c = 0.15$, and $\alpha = 0°$ demonstrating pre-bifurcation, mode A, and mode B flow fields. In Figure 5 these are in the form of time-averaged velocity magnitude. Figure 5a, for a pre-bifurcation flow field, clearly shows a

time-averaged jet aligned horizontally. The associated phase-averaged vorticity fields in Figure 6 (left column) demonstrate this jet to be the result of a reverse-Kármán vortex street. During the downward motion (a to c) a counter-clockwise vortex forms and sheds from the trailing-edge; during the upward motion (c to a) a clockwise vortex forms and sheds. Both of these vortices convect along a path approximately aligned with the horizontal with equidistant spacing. At the leading-edge an upper surface clockwise vortex forms during the downward motion (see c) and is dissipated during the upward motion through impingement with the upward moving airfoil as previously described by Visbal (2009) and Cleaver et al. (2009a). Conversely during the upward motion a counter-clockwise leading-edge vortex forms (see a) which is dissipated during the downward motion. The flow field as a whole is characterized by symmetry about the horizontal plane justifying the near-zero time-averaged lift coefficient.

With the Strouhal number increased into the dual-flow regime this symmetry is broken, see Figures 5b and 5c. For mode A the time-averaged jet is deflected upwards and there is a high velocity region over the upper surface. For mode B the inverse is true, a downwards deflected jet and a high velocity leading-edge region over the lower surface. The phase-averaged vorticity shown in Figure 6 identifies the cause to be trailing-edge vortex dipole formation. For mode A (centre column) the clockwise trailing-edge vortex (TEV) forms during the upward motion (c to a) and 'loiters' near the airfoil during the downward motion (a to c) during which the counter-clockwise TEV forms. As a result of their proximity the vortices form a dipole that due to the relative positions of the vortices has a self-induced velocity in the upwards direction, thereby creating an upwards deflected jet. For mode B (right column) the inverse is true, i.e., the counter-clockwise TEV loiters, creating a vortex dipole with a downwards self-induced velocity and therefore a downwards deflected jet. The

mode B flow field therefore appears mirrored in the horizontal and 180 degrees out of phase with the mode A flow field, compare Figure 6c (centre) with Figure 6a (right).

Due to the asymmetry of the flow near the trailing-edge, asymmetry is also created near the leading-edge. Mode A has a strong upper surface LEV (Figure 6c centre), and comparatively weak lower surface LEV (Figure 6a centre), explaining both the high time-averaged velocity above the upper surface observed in Figure 5b and also the very high positive time-averaged lift coefficient, $c_l \approx 3.4$. For mode B the inverse is true, i.e., a weak upper surface LEV and strong lower surface LEV resulting in a large negative lift coefficient. Hence, the lift direction is the same as the direction of the vertical component of the deflected jet. This is consistent with the simulations performed at much lower Reynolds numbers (Re = 200 in Emblemsvag et al. 2002; Re = 1,850 in Liang et al. 2011).

Both Figure 5 and 6 are for zero degree angle of attack where symmetry about the horizontal plane simplifies the problem. However, as suggested by the force data shown in Figure 4, similar dual flows exist for nonzero angles of attack. Figure 7 therefore shows phase-averaged vorticity contours for mode A and Figure 8 for mode B for the three angles of attack that exhibit dual flows. In both figures the left column is the top of the motion and the right the bottom. For mode A, Figure 7 shows that qualitatively the wake structure is independent of angle of attack in this range. In all cases there is a TEV dipole, which, due to the vortex positions, convects upwards. For mode B Figure 8 shows that the same is true except the wake structure is inverted. There is a vortex dipole at the top of the motion which convects downwards to create a downwards deflected jet. It can therefore be concluded that the same phenomenon, deflected jets, is responsible for the lift force bifurcations observed for $\alpha \leq 10°$.

It is interesting to note that an upwards deflected jet (mode A) is associated with high lift for $\alpha = 10°$ in Figure 4 and a downwards deflected jet (mode B) is associated with low (and

even negative) lift. This relationship between the direction of the lift and deflected jet is contrary to what one would intuitively expect based on a simple control volume argument. As the deflected jet has a momentum, one would expect a reaction force opposite to its direction, hence lift is expected to be opposite to the direction of the deflected jet. Although momentum in the deflected jet may make a small contribution to the lift force, the lift force is instead dominated by the effect the deflected jet has on the flow over the airfoil surfaces, i.e., the region of high velocity flow over the upper / lower surface in Figure 5.

3.4 Effect of initial conditions

The initial conditions can be divided into two broad categories: increasing and decreasing frequency. For increasing frequency, the starting position is always the stationary case, and the result is the same, mode A, for all three angles of attack. This is unexpected for $\alpha = 0°$, as symmetry means that logically mode B is equally likely. Practically however symmetry is impossible to achieve experimentally, and in practice the mode B case only occurred once in twelve occasions (and is therefore not presented here). From this it can be concluded that for increasing frequency the direction of the deflected jet is extremely susceptible to even slight asymmetry.

For decreasing frequency the situation is more complicated. For $\alpha = 0°$, symmetry means either case is equally possible and it has previously been shown (von Ellenrieder & Pothos, 2008) that starting position is the determining factor. This is further complicated because there are an infinite number of possible starting positions in the range $-a \leq h_i \leq a$, and because experimentally a true impulsive start (meaning an infinite acceleration to full frequency) is not physically possible. For the purposes of this study the acceleration time is measured to be less than the full period as demonstrated in the insets of Figure 9 and Figure 10, and only the two extreme starting positions are considered in detail: $h_i = a$, and $-a$. The

effect of these starting positions on whether mode A or B is produced is shown in Table 1. These are derived from ten repeats for each starting position. For all angles of attack and amplitudes starting with a position of $h_i = -a$, produces mode B (downwards deflected jet). Starting with a position of $h_i = a$ is more complicated. For $\alpha = 0°$ and 5° this starting position consistently produces mode A (upwards deflected jet), but at $\alpha = 10°$ it only produces an upwards deflected jet at a single amplitude and only 20% of the time. In all other cases a mode B case is produced. This suggests that the direction of the deflected jet is determined by competing asymmetries, i.e., starting position versus angle of attack. It is important to note that for $\alpha > 0°$ in Figures 4, 7 and 8 a starting position of $h_i = 0$ (up) was used to guarantee a mode B flow field.

Table 1. Effect of starting position on the mode produced.

	Angle of Attack, α:	**0°**	**5°**	**10°**		
	a/c:	**0.15**	**0.15**	**0.10**	**0.15**	**0.20**
Starting Position, h_i	**a**	**A**	**A**	**B**	**B (80%)**	**B**
	-a	**B**	**B**	**B**	**B**	**B**

To investigate how starting position and angle of attack influence the direction of the deflected jet, phase-locked instantaneous PIV measurements were performed for the first five cycles of an impulsive start from $h_i = a$ with $a/c = 0.15$, $\alpha = 0°$ and $\alpha = 10°$, see Figure 9. For $\alpha = 0°$ a mode A (upward jet) is produced, and for $\alpha = 10°$ a mode B (downward jet) is produced. In this figure, instantaneous velocity field is shown in each image when the airfoil is at the bottom of the motion. For $\alpha = 0°$, the first counter-clockwise TEV can be seen above the trailing-edge in Figure 9a (left), and can again be seen below the vortex dipole in Figure 9b (left). This vortex dipole is formed from the first clockwise TEV and second counter-clockwise TEV, and due to the vortex positions convects upwards creating an upwards deflected jet. As only two trailing-edge vortices are created in each cycle, one clockwise and

one counter-clockwise, all future cycles will now be ‘locked-in’ to this mode of vortex pairing creating a stable upwards deflected jet, see Figure 9c through e (left). The starting process for $\alpha = 10°$ is shown in the right column of Figure 9. As before a counter-clockwise vortex forms during the first downward motion but in this case it is only partially visible at the bottom of Figure 9b where it appears to have paired with the first clockwise TEV. In Figure 9c to e the flow field is now clearly representative of a stable downwards deflected jet. From Figure 9 it can be concluded that the direction of the deflected jet is determined in the first two cycles, and the motion of the first counter-clockwise trailing-edge vortex is crucial.

To give more detail of the startup process, shown in Figure 10 is selected instantaneous PIV images from the first two cycles. For $\alpha = 0°$ the first counter-clockwise vortex can be seen as CCW1 in A, and then again at the top of the next cycle next to the first clockwise vortex (CW1) in B. During the course of the next cycle it can be seen that the first counter-clockwise vortex has little effect on the outcome as the first clockwise vortex pairs with the second counter-clockwise vortex instead. As a result the first vortex dipole convects upwards. By contrast for $\alpha = 10°$ the first clockwise vortex pairs with the first counter-clockwise vortex drawing it downwards, see B through F (right). This results in a flow field, where the counter-clockwise TEV ‘loiters’ and pairs with the clockwise TEV to give a downwards deflected jet. The reason for the increased effect of the first counter-clockwise vortex at $\alpha = 10°$ is its increased strength. This is quantified through the absolute circulation measurements shown in Figure 11. For $\alpha = 0°$ (solid lines), there is a very large difference between the circulation of the first counter-clockwise and clockwise TEV. This is due to the aforementioned acceleration time which results in the airfoil moving slower in the first downwards motion than the first upwards. For $\alpha = 10°$ the gap in vortex strengths is reduced due to the positive bias in the effective angle of attack. This enables the first clockwise TEV

to pair with the first counter-clockwise and therefore create a downward deflected jet. It is therefore important to note that different acceleration rates could cause different results.

3.5 Effect of amplitude

Shown in Figure 12 is time-averaged lift coefficient for five amplitudes, at four angles of attack $\alpha = 0°$, 5°, 10°, and 15°. Figure 12a shows the data for $\alpha = 0°$; and for each amplitude three initial conditions are considered: increasing frequency, decreasing frequency with $h_i = a$, and decreasing frequency with $h_i = -a$. Both $a/c = 0.025$ and 0.050 do not exhibit bifurcation behavior. For $a/c \geq 0.10$ however bifurcation behavior is evident. For all three amplitudes initially the three curves match following $c_l \approx 0$. Then at a critical Strouhal number these three curves bifurcate with increasing and decreasing ($h_i = a$) frequency consistently becoming mode A, and decreasing ($h_i = -a$) consistently becoming mode B. The Strouhal number of the onset of bifurcation is delayed by smaller amplitude, hence the bifurcation occurs at $St_c = 1.25$, 1.50, and 2.00 for $a/c = 0.20$, 0.15, and 0.10 respectively. Similarly for $\alpha = 5°$ and 10° (see Figures 12b and 12c), bifurcation only occurs for $a/c \geq 0.10$, with increasing frequency becoming mode A and decreasing frequency becoming mode B. Again the point of bifurcation is amplitude dependent but slightly delayed from that for $\alpha = 0°$. The bifurcation points for $\alpha = 5°$ are therefore $St_c = 1.30$, 1.58, and 2.00 for $a/c = 0.20$, 0.15, and 0.10 respectively; and for $\alpha = 10°$ are $St_c = 1.30$, 1.58, and 2.10 for a/c = 0.20, 0.15, and 0.10 respectively. These points are however approximate as how to define the bifurcation point is subjective and therefore accurate to one measurement interval. For $\alpha = 15°$ across all amplitudes there is no significant bifurcation. There is some minor hysteresis at the higher Strouhal numbers as previously described for $a/c = 0.15$ but this behavior is not indicative of dual flows.

The time-averaged drag coefficient for the same cases as in Figure 12 is shown in Figure 13. For $\alpha = 0°$ (Figure 13a), generally there is decreasing drag coefficient with increasing Strouhal number, with greater effect for greater amplitude as predicted by Garrick approximations and previously observed in other studies (Jones & Platzer, 1997; Tuncer & Platzer, 2000; Young & Lai, 2004). For this angle of attack for all amplitudes all three curves (increasing and decreasing frequency) match to within the bounds of experimental uncertainty across the entire Strouhal number range. Hence, there is no sign of the bifurcation behavior observed in the associated lift coefficient (Figure 12a). This is a consequence of the symmetry at $\alpha = 0°$ which means that in terms of horizontal force there is no difference between upwards / downwards deflected jet because they are mirror images of each other in the horizontal plane and therefore create the same horizontal force component. With the angle of attack increased to $\alpha = 5°$ this symmetry is broken and a bifurcation is therefore observed, see Figure 13b. As observed in the lift coefficient, this only occurs for $a/c \geq 0.10$, and is amplitude dependent with the onset being at the same Strouhal numbers as observed in the lift coefficient. As a result of the bifurcation, the decreasing frequency case (downwards deflected jet) consistently produces more thrust. The thrust enhancing nature of the downwards deflected jet is a result of the strong lower surface vortex which acts on the forward facing lower surface of the airfoil. The magnitude of this difference in drag is small in comparison with that observed in the lift coefficient, i.e., $\Delta c_d \approx 0.5$ versus $\Delta c_l \approx 7.0$. Increasing the angle of attack to $\alpha = 10°$ amplifies this difference, $\Delta c_d \approx 0.75$. The onset of bifurcation is again amplitude dependent reflecting the points observed in the lift coefficient. With the angle of attack increased to $\alpha = 15°$ (Figure 13d), there is no longer a bifurcation at any amplitude, again reflecting the trends observed in lift coefficient.

To confirm that deflected jets are responsible for the force bifurcations at all amplitudes phase-averaged vorticity contour plots at the top (left) and bottom (right) of the motion for

a/c = 0.10, 0.15, and 0.20 are shown in Figure 14 and 15 for α = 0°. The Strouhal numbers are the maximum tested in the force measurements and therefore demonstrate post-bifurcation wakes. Figure 14 is for the mode A and therefore demonstrates an upwards deflected jet as is visible in the right column. Figure 14 also excellently demonstrates the previously discussed LEV asymmetry, compare the weak lower surface LEV in the left column with the strong upper surface LEV in the right column. The only significant difference between amplitudes is the increased spacing between the TEVs in the dipole with increasing amplitude, see right column. For the mode B case shown in Figure 15 the inverse is generally true, i.e., the jet is deflected downwards and the lower surface LEV is the stronger. Across all amplitudes the cause of the force bifurcation is therefore the same phenomenon, which is deflected jets.

As further confirmation of the existence of deflected jets for all cases where bifurcation occurs, the angle of the deflected jet was measured by tracking the motion of the trailing-edge vortices in phase-averaged PIV measurements. Figure 16a for α = 0° reaffirms that in the pre-bifurcation regime the vortices convect approximately horizontally. After bifurcation, for mode A, the vortex trajectory angle becomes negative indicative of an upwards deflected jet, for mode B the vortex trajectory angle becomes positive indicative of a downward deflected jet. Figure 16b and 16c confirm similar trends for α = 5° and α = 10° but with a bias towards positive vortex trajectory angles due to the nonzero angle of attack.

3.6 Bifurcation criteria

In this section several criteria to predict the onset of bifurcation shall be introduced. To this end shown in Figure 17 are the points of bifurcation in the amplitude-Strouhal number domain. Also shown is a power law curve fit of the drag to thrust switch points as derived from Figure 13. These show that the location of the switch from drag to thrust is highly

amplitude dependent with earlier zero drag for greater amplitude. The point of zero drag is also delayed by increasing angle of attack, mostly due to the increased drag of the stationary airfoil which must be overcome, but also to a lesser extent by the drag enhancing effect of the convecting upper surface vortex acting on the rearward facing upper surface. The single-dual flowfield boundary is likewise delayed to higher Strouhal numbers by increasing angle of attack but the effect is not as pronounced. Extrapolation of these curves to smaller amplitudes and higher Strouhal numbers shows that dual-flow was not observed at the smaller amplitudes (a/c = 0.025 and a/c = 0.05) because the maximum Strouhal number studied was insufficient.

The trend of increasing Strouhal number with decreasing amplitude suggests the possibility of a constant plunge velocity or effective angle of attack as criteria for the onset of bifurcation. Figure 18 therefore shows the bifurcation onset points as symbols plotted against both Strouhal number based on amplitude and effective angle of attack. Effective angle of attack varies in a range so the limits of this range ($\alpha_{eff,min}$ and $\alpha_{eff,max}$) are used in Figure 18. The points representing the onset of bifurcation fall within the range $St_A = 0.45 \pm 0.05$ which is in very close agreement with the range $0.434 < St_A < 0.455$ suggested by von Ellenreider and Pothos (2008). The trend of decreasing St_A with decreasing amplitude and angle of attack means however that this cannot be considered a universal criterion. In terms of effective angle of attack the points fall within the range $\alpha_{eff,max} = 60° \pm 9°$, however again due to the trend of decreasing effective angle of attack with amplitude and angle of attack this cannot be considered a universal criterion. In addition, neither plunge velocity nor effective angle of attack gives an adequate explanation as to why there is no bifurcation at larger angles of attack ($\alpha > 10°$).

As a simple universal criterion cannot be defined from the controllable experimental parameters it is necessary instead to derive a criterion from the flow field measurements. As

deflected jets are a direct result of TEV dipole formation the logical choice is a criterion based around the strength of the trailing-edge vortices. Shown in Figure 19 is therefore the circulation of the TEVs for α = 0°, 5°, 10° and 15°, for *a/c* = 0.05, 0.10, 0.15, and 0.20. Clockwise TEVs are denoted by solid lines and counter-clockwise TEVs by dashed lines. The pre-bifurcation case is denoted by solid symbols, with the mode A treated as a continuation of this, and the mode B denoted by open symbols. For α = 0° both trailing-edge vortices grow almost identically with increasing Strouhal number until the point of bifurcation. After the point of bifurcation the asymmetric wake creates asymmetry in the strengths of the clockwise and counter-clockwise vortices. For mode A the clockwise vortex becomes stronger than the counter-clockwise vortex, and vice-versa for mode B. There is a strong amplitude dependence of the trailing-edge vortex strength. For α = 5° the same basic trend is observed except that the clockwise circulation curve is shifted downwards and the counter-clockwise curve is shifted upwards. This is due to the greater mean angle of attack causing greater asymmetry in the effective angle of attack as demonstrated in Figure 18. The gap between clockwise and counter-clockwise vortex is further enhanced by α = 10°.

For α = 15° this trend of increased counter-clockwise vortex circulation and reduced clockwise trailing-edge vortex circulation is continued, however now only a single mode is observed, one with a stronger counter-clockwise vortex than clockwise vortex. The circulation measurements for the smaller angles of attack demonstrate that this is typical of a mode B flow field. Indeed when comparing the flow field for α = 15° with the mode B flow field for α = 5° and α = 10° (see Figure 20), it bears all the hallmarks of a mode B flow field and yet without a point of bifurcation it is not possible to classify it as such. In summary, the increasing angle of attack causes greater asymmetry in the effective angle of attack which causes an imbalance in the trailing-edge vortex strengths, inclining the wake towards a

downward deflected jet. To characterize this asymmetry a new parameter is suggested based on the angular velocity of a vortex pair (Milne-Thomson, 1968):

$$\frac{(\Gamma_{T+} + \Gamma_{T-})}{d^2} \tag{5}$$

where d is the distance between the vortices. This is made dimensionless as:

$$\frac{(\Gamma_{T+} + \Gamma_{T-})c}{U_\infty d^2} \quad . \tag{6}$$

This represents a non-dimensional trailing-edge vortex *asymmetry parameter*. Our data suggests that the mode A flow field is not possible once this asymmetry parameter exceeds a critical value, as will be discussed further.

In a similar manner, it is possible to consider the minimum plunge velocity criteria in terms of the experimentally measured circulation. Shown in Figure 21 is the average absolute circulation of the two trailing-edge vortices versus Strouhal number. The average circulation is used so as to minimize and separate out any asymmetry effects. For the different angles of attack the curves collapse onto a nearly parabolic trend with the gradient determined by the amplitude. The points of bifurcation are identified through the grey dashed line. This shows that a minimum threshold trailing-edge vortex circulation is required for bifurcation to occur. The trend with amplitude suggests that bifurcation requires larger trailing-edge vortex circulation at larger amplitudes. This is rational since larger amplitude leads to larger trailing-edge vortex spacing which inhibits vortex-pairing. If this trend is extrapolated to higher St_c, it is clear that for a/c = 0.05 the level of trailing-edge vortex circulation is insufficient for bifurcation (within the Strouhal number range tested).

Combining both the asymmetry parameter and the normalized circulation parameter produces Figure 22. A horizontal boundary separating the single and dual modes is shown; and a vertical boundary separating mode A and mode B is revealed. The question of why there is no bifurcation at low amplitudes is therefore answered by the circulation threshold,

and the question of why there is no mode A at large angles of attack is answered by the asymmetry boundary, i.e., all the points for α = 15° lie to the mode B side of the boundary.

The threshold circulation displayed in Figure 22 is however not perfect, as seen by the scatter. As the airfoil is in effect acting as a vortex generator with the strength determined by the plunge velocity, plunge velocity is a more logical normalizing variable. Shown in Figure 23 is this alternative circulation parameter with the same asymmetry parameter. As expected the data points have collapsed down to a smaller band, but more importantly there is now a clear boundary between the single and dual modes with minimal scatter of the data. The critical value of circulation normalized by plunge velocity corresponding to the bifurcation points is $\overline{\Gamma}/U_P c$ = 1.85. When compared to Figure 22 the collapse of the data into a smaller band in Figure 23 elucidates the importance of plunge velocity.

Alternatively, Figure 24 shows all the trailing-edge vortex circulations for all amplitudes and angles of attack plotted against St_A. This figure demonstrates the three possible bifurcation criteria: St_A = 0.45±0.05 on the x-axis, $\overline{\Gamma}/U_\infty c$ = 2.6±0.3 on the y-axis, and $\overline{\Gamma}/U_P c$ = 1.85 as a straight line with its gradient determined by:

$$\frac{\overline{\Gamma}}{U_P c} = \frac{\overline{\Gamma}}{\pi U_\infty St_A c} = 1.85 \tag{7}$$

therefore,

$$\frac{\overline{\Gamma}}{U_\infty c} = 1.85\pi St_A \tag{8}$$

This line passes through the points of bifurcation with the values above being dual mode and the values below single mode. Hence, this reinforces the significance of plunge velocity in determining the trailing-edge vortex strength.

The circulation normalized by the plunge velocity, $\Gamma/U_p c$, can be also interpreted as the inverse of a modified Strouhal number based on the dipole velocity Γ/a, the frequency and chord length. Initial distance between the trailing-edge vortices of opposite sign is on the order of peak-to-peak amplitude $2a$. This is physically more meaningful than the distance

once the dipole is formed. In summary, the strength parameter can also be viewed as the inverse of a modified Strouhal number (which is the ratio of two time scales).

3.7 Effect of Reynolds number

All the results presented for plunging airfoil so far were for Re = 10,000. Figure 25 shows the effect of Reynolds numbers in the range Re = 2,500 to 15,000 on an upward deflected jet. Although there are minor differences in the shape and size of some of the vortices the wake as a whole is very similar, and crucially the deflected jet is still apparent for all Reynolds numbers. We found that bifurcation occurs for St_c = 2.00-2.25 for $\alpha = 0°$ and a/c = 0.15. The phenomenon of deflected jets and their associated force bifurcations are therefore applicable to a wide range of Reynolds numbers.

4. Conclusions

Time-averaged force measurements on a periodically plunging NACA 0012 airfoil have identified significant bifurcations at high Strouhal numbers for angles of attack smaller than and equal to the stall angle. These bifurcations were observed when the frequency of the oscillations was increased slowly up to a maximum value and the motion was stopped, and then restarted impulsively at the maximum frequency and the frequency was decreased very slowly. It was found that below a critical frequency, lift force and flow fields were identical; however, above this bifurcation frequency, dual flows and significantly different lift forces were observed. These dual flows were characterized as thrust producing deflected jets. Trailing-edge vortex loiters over the airfoil forming a vortex dipole with the opposite sign vortex to produce deflected jets, which also modify the leading-edge vortices and may produce very high lift coefficients. The lift direction is the same as the direction of the vertical component of the deflected jet. The direction of these deflected jets is determined by

the initial conditions and the angle of attack. The direction of the deflected jets is determined in the first two cycles by the first trailing-edge vortex. Following an impulsive start, a stable flow is established in approximately two plunging cycles. Bifurcation and deflected jets were observed in a wide range of Reynolds numbers.

Effective angle of attack due to the plunging motion or the Strouhal number based on amplitude has some correlation to the onset of bifurcation. However, better correlations and insight to flow physics were derived from the flow field measurements. Analysis of the trailing edge vortices lead to two parameters which describe the wake behavior. Firstly, an asymmetry parameter is derived from the difference in circulation of the clockwise and counter-clockwise trailing-edge vortex. This parameter determines whether the deflected jet is deflected upwards or downwards. It also explains why dual flows are not observed at larger angles of attack as the greater asymmetry in the effective angle of attack causes an imbalance in the trailing-edge vortex strengths, which gives a natural tendency towards a downwards deflected jet. Secondly, a strength parameter is derived from the average of the circulations of the trailing edge vortices. From the measured values of circulation, this parameter can be expressed as circulation normalized by the freestream velocity or circulation normalized by the plunge velocity. It was shown that a minimum value of the strength parameter is necessary for bifurcation to occur. The bifurcation was therefore not observed at small amplitudes or low frequencies, due to insufficient trailing-edge vortex strength. Circulation normalized by the plunge velocity gives the best data collapse, which can be interpreted as the inverse of a modified Strouhal number.

This work was sponsored by the Air Force Office of Scientific Research, Air Force Material Command, USAF under grant number FA8655-10-1-3093, monitored by Dr. D.

Smith, as well as the Engineering and Physical Sciences Research Council (EPSRC) Studentship, and the RCUK Academic Fellowship in Unmanned Air Vehicles.

REFERENCES

BOHL D. G.&KOOCHESFAHANI M. M. 2009 MTV measurements of the vortical field in the wake of an airfoil oscillating at high reduced frequency. *J. Fluid Mech.* **620**, 63-88.

BRATT J. B. 1950 Flow patterns in the wake of an oscillating airfoil. *Aeronautical Research Council,* R & M 2773.

CLEAVER D. J., WANG Z.&GURSUL I. 2011 Lift Enhancement by means of small amplitude airfoil oscillations at low Reynolds numbers. *AIAA J.* **in print**,

CLEAVER D. J., WANG Z. J.&GURSUL I. 2009a Delay of Stall by Small Amplitude Airfoil Oscillation at Low Reynolds Numbers. *AIAA Paper 2009-392*.

CLEAVER D. J., WANG Z. J.&GURSUL I. 2009b Lift Enhancement on Oscillating Airfoils. *AIAA Paper 2009-4028*.

EMBLEMSVAG J. E., SUZUKI R.&CANDLER G. 2002 Numerical simulation of flapping micro air vehicles. *AIAA Paper 2002-3197*.

FRAMPTON K. D., GOLDFARB M., MONOPOLI D.&CVETICANIN D. 2002 Passive aeroelastic tailoring for optimal flapping wings. In *Fixed and Flapping Wing Aerodynamics for Micro Air Vehicle Applications*, (ed. TJ Mueller),pp 473-82.Amer Inst Aeronautics & Astronautics.

GODOY-DIANA R., AIDER J. L.&WESFREID J. E. 2008 Transitions in the wake of a flapping foil. *Phys. Rev. E* **77**,

GODOY-DIANA R., MARAIS C., AIDER J. L.&WESFREID J. E. 2009 A model for the symmetry breaking of the reverse Benard-von Karman vortex street produced by a flapping foil. *J. Fluid Mech.* **622**, 23-32.

GRAFTIEAUX L., MICHARD M.&GROSJEAN N. 2001 Combining PIV, POD and vortex identification algorithms for the study of unsteady turbulent swirling flows. *Meas. Sci. Technol.* **12**, 1422-29.

HEATHCOTE S.&GURSUL I. 2007a Flexible flapping airfoil propulsion at low Reynolds numbers. *AIAA J.* **45**, 1066-79.

HEATHCOTE S.&GURSUL I. 2007b Jet switching phenomenon for a periodically plunging airfoil. *Phys Fluids* **19**,

HO S., NASSEF H., PORNSINSIRIRAK N., TAI Y. C.&HO C. M. 2003 Unsteady aerodynamics and flow control for flapping wing flyers. *Prog. Aerosp. Sci.* **39**, 635-81.

HUANG R. F.&LIN C. L. 1995 Vortex Shedding and Shear-Layer Instability of Wing at Low-Reynolds Numbers. *AIAA J.* **33**, 1398-403.

JONES K. D., DOHRING C. M.&PLATZER M. F. 1998 Experimental and computational investigation of the Knoller-Betz effect. *AIAA J.* **36**, 1240-46.

JONES K. D.&PLATZER M. F. 1997 Numerical Computation of Flapping-Wing Propulsion and Power Extraction. *AIAA Paper 97-0826*.

LEWIN G. C.&HAJ-HARIRI H. 2003 Modelling thrust generation of a two-dimensional heaving airfoil in a viscous flow. *J. Fluid Mech.* **492**, 339-62.

LIANG C. L., OU K., PREMASUTHAN S., JAMESON A.&WANG Z. J. 2011 High-order accurate simulations of unsteady flow past plunging and pitching airfoils. *Computers & Fluids* **40**, 236-48.

MILNE-THOMSON L. M. 1968 *Theoretical Hydrodynamics*. The Macmillan Press Ltd.

MOFFAT R. J. 1988 Describing the Uncertainties in Experimental Results. *Exp. Therm. Fluid Sci.* **1**, 3-17.

MORGAN C. E., BABINSKY H.&HARVEY J. K. 2009 Vortex Detection Methods for use with PIV and CFD data. *AIAA Paper 2009-74*.

PLATZER M. F., JONES K. D., YOUNG J.&LAI J. C. S. 2008 Flapping-wing aerodynamics: Progress and challenges. *AIAA J.* **46**, 2136-49.

SANE S. P. 2003 The aerodynamics of insect flight. *J. Exp. Biology* **206**, 4191-208.

SCHLUTER J. U. 2009 Lift Enhancement at Low Reynolds Numbers using Pop-up Feathers. *AIAA Paper 2009-4195*.

SHYY W., BERG M.&LJUNGQVIST D. 1999 Flapping and flexible wings for biological and micro air vehicles. *Prog. Aerosp. Sci.* **35**, 455-505.

SUNADA S., SAKAGUCHI A.&KAWACHI K. 1997 Airfoil section characteristics at a low Reynolds number. *J. of Fluids Eng. - Trans. of the ASME* **119**, 129-35.

TRIANTAFYLLOU M. S., TRIANTAFYLLOU G. S.&YUE D. K. P. 2000 Hydrodynamics of fishlike swimming. *Ann. Rev. Fluid Mech.* **32**, 33-53.

TUNCER I. H.&PLATZER M. F. 2000 Computational study of flapping airfoil aerodynamics. *J. of Aircraft* **37**, 514-20.

VISBAL M. R. 2009 High-Fidelity Simulation of Transitional Flows past a Plunging Airfoil. *AIAA J.* **47**, 2685-97.

VON ELLENRIEDER K. D.&POTHOS S. 2008 PIV measurements of the asymmetric wake of a two dimensional heaving hydrofoil. *Exp. Fluids* **44**, 733-45.

WANG Z. J. 2000 Two dimensional mechanism for insect hovering. *Phys. Rev. Lett.* **85**, 2216-19.

YOUNG J.&LAI J. C. S. 2004 Oscillation frequency and amplitude effects on the wake of a plunging airfoil. *AIAA J.* **42**, 2042-52.

FIGURES

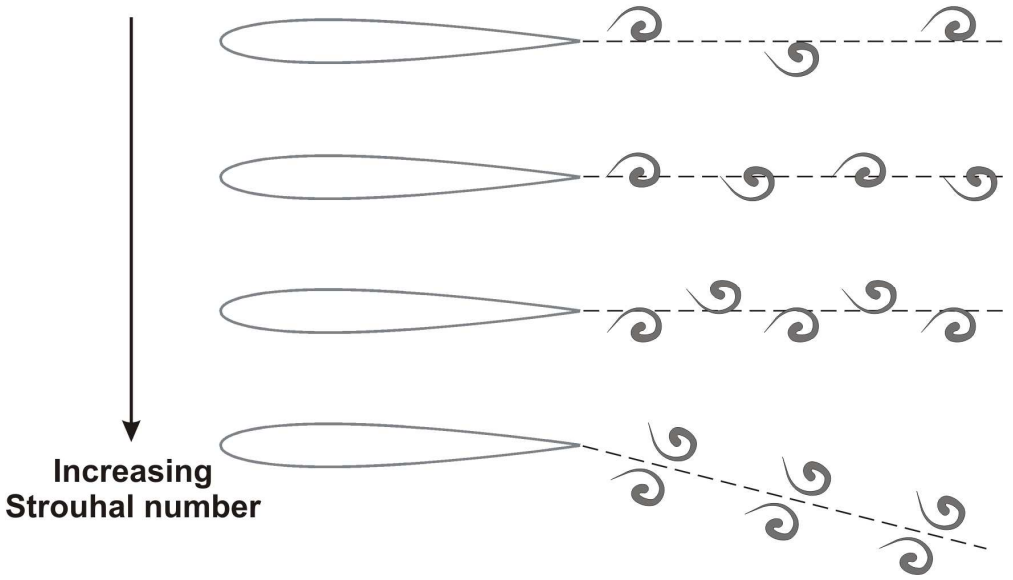

FIGURE 1. Wake patterns with increasing Strouhal number. In descending order: drag producing wake, neutral wake, thrust producing wake, and deflected wake.

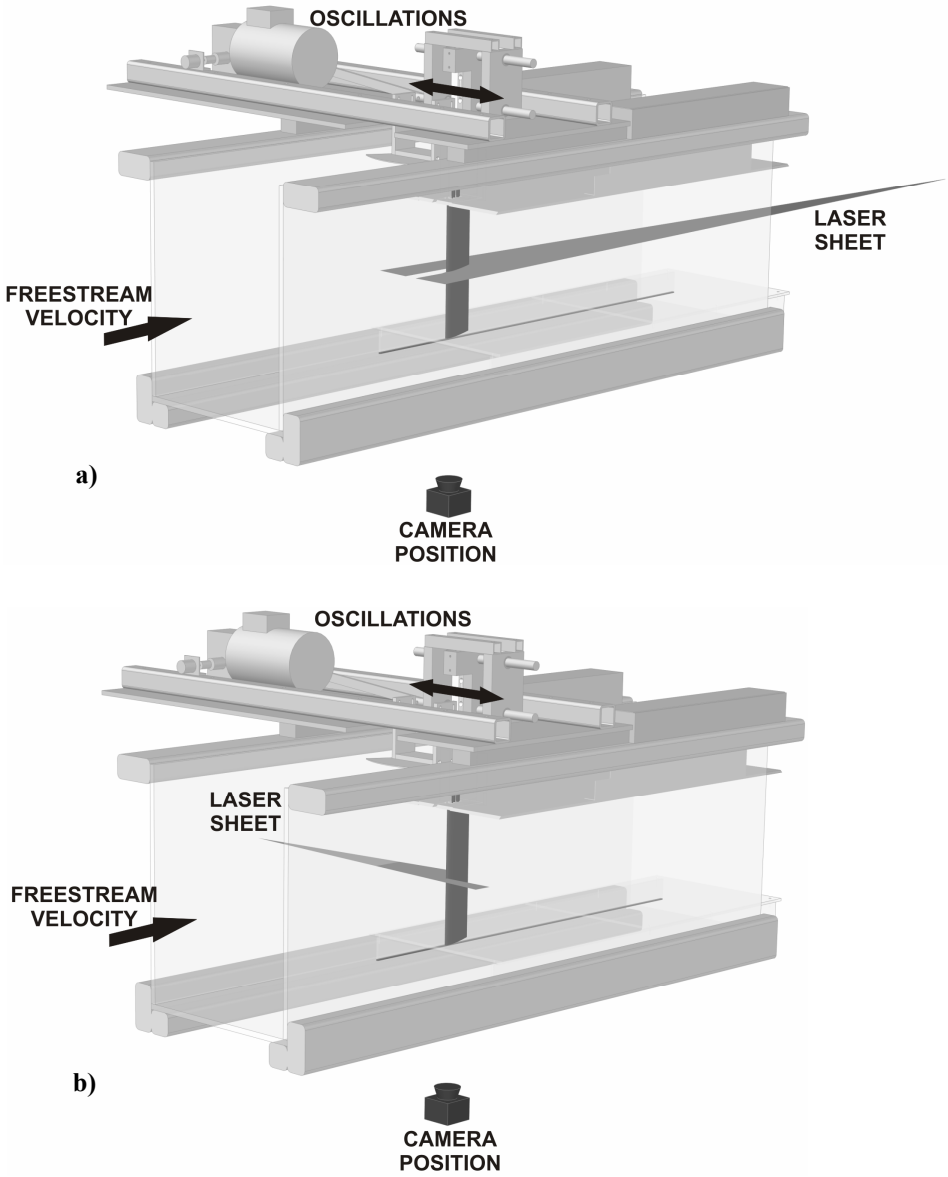

FIGURE 2. Experimental setup a) for PIV measurements over the upper surface, and b) for PIV measurements over the lower surface.

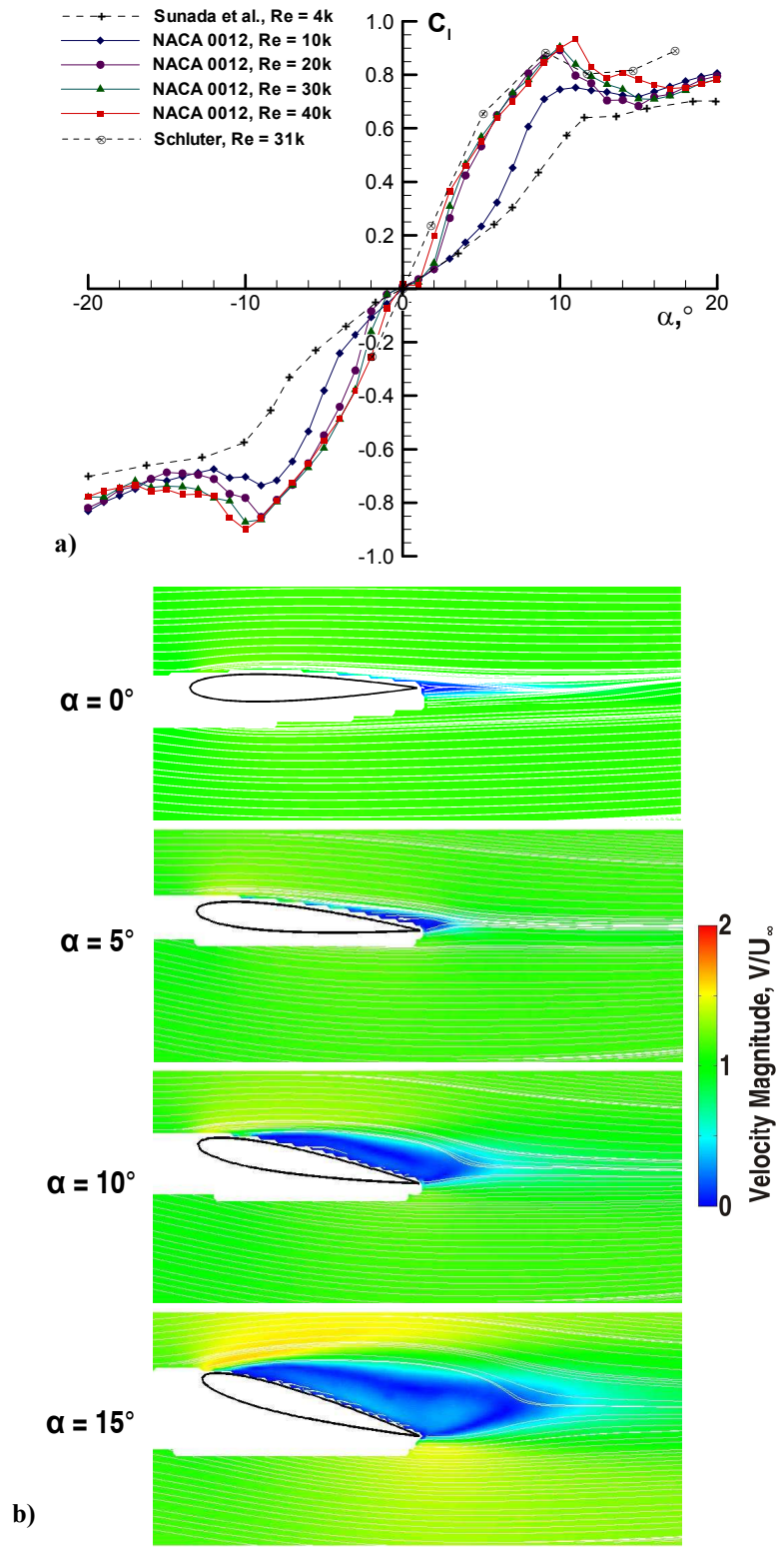

FIGURE 3. a) Lift coefficient for the stationary airfoil and, b) associated time-averaged velocity magnitude for the four angles of attack under consideration for *Re* = 10,000.

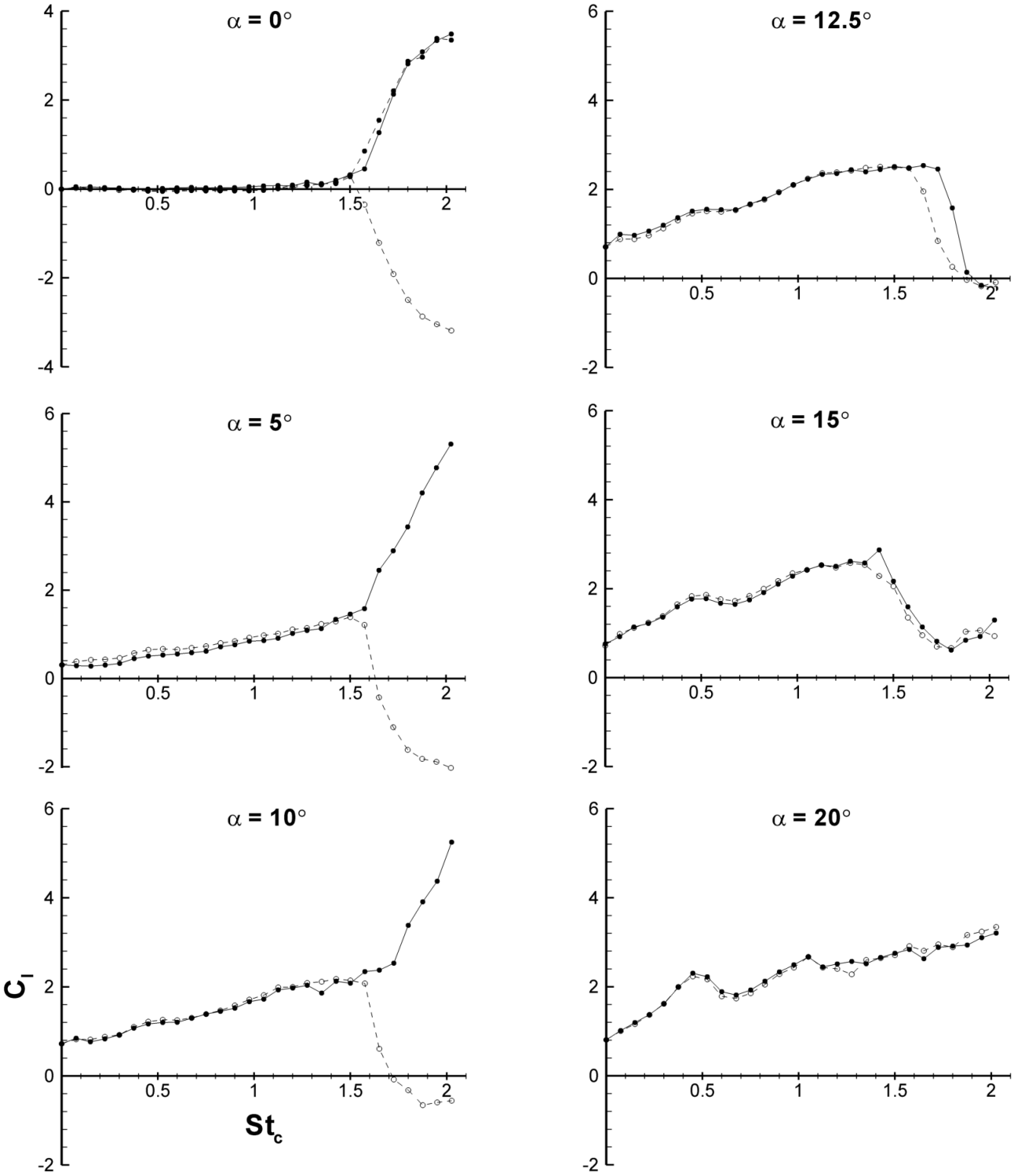

FIGURE 4. Time-averaged lift coefficient for a/c = 0.15 and all angles of attack considered. Solid line represents increasing frequency, dashed line represents decreasing frequency with a starting position for $\alpha = 0°$ of $h_i = \pm a$, and for $\alpha > 0°$ $h_i = 0$ (airfoil moving upwards).

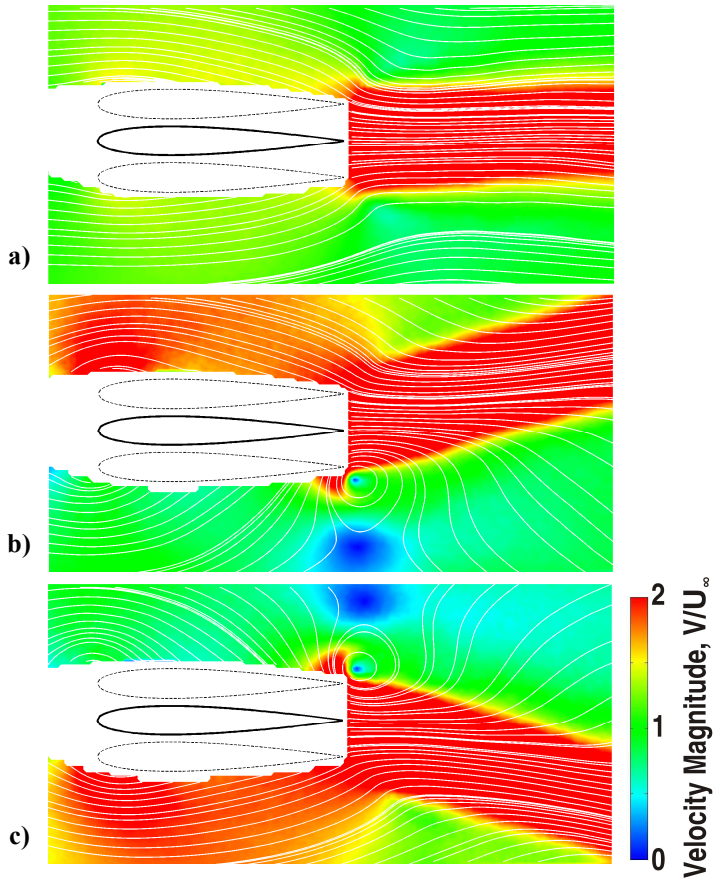

FIGURE 5. Time-averaged velocity magnitude for a/c = 0.15, α = 0°, and: a) St_c = 1.500 - pre-bifurcation, b) St_c = 2.025 – mode A, and c) St_c = 2.025 – mode B.

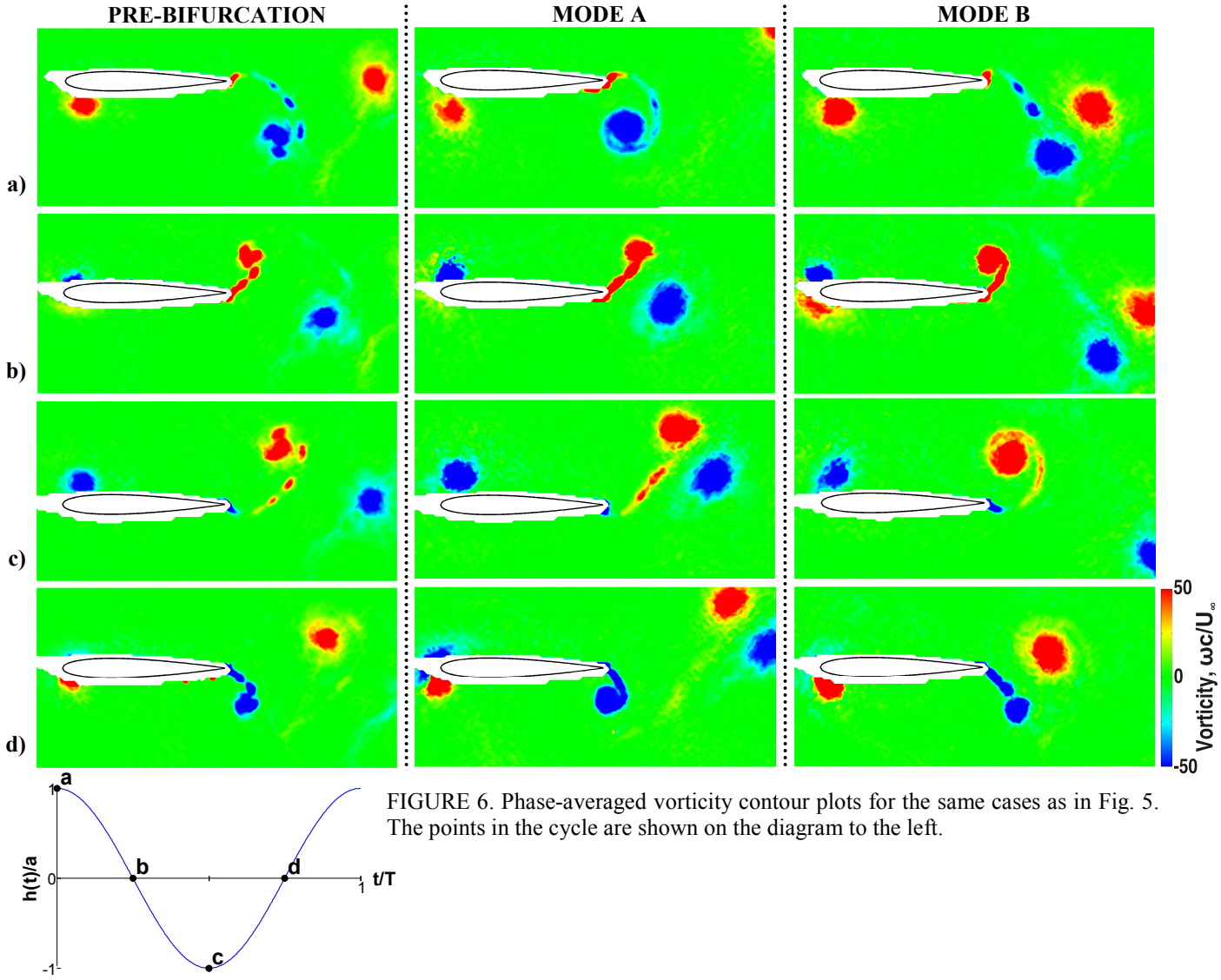

FIGURE 6. Phase-averaged vorticity contour plots for the same cases as in Fig. 5. The points in the cycle are shown on the diagram to the left.

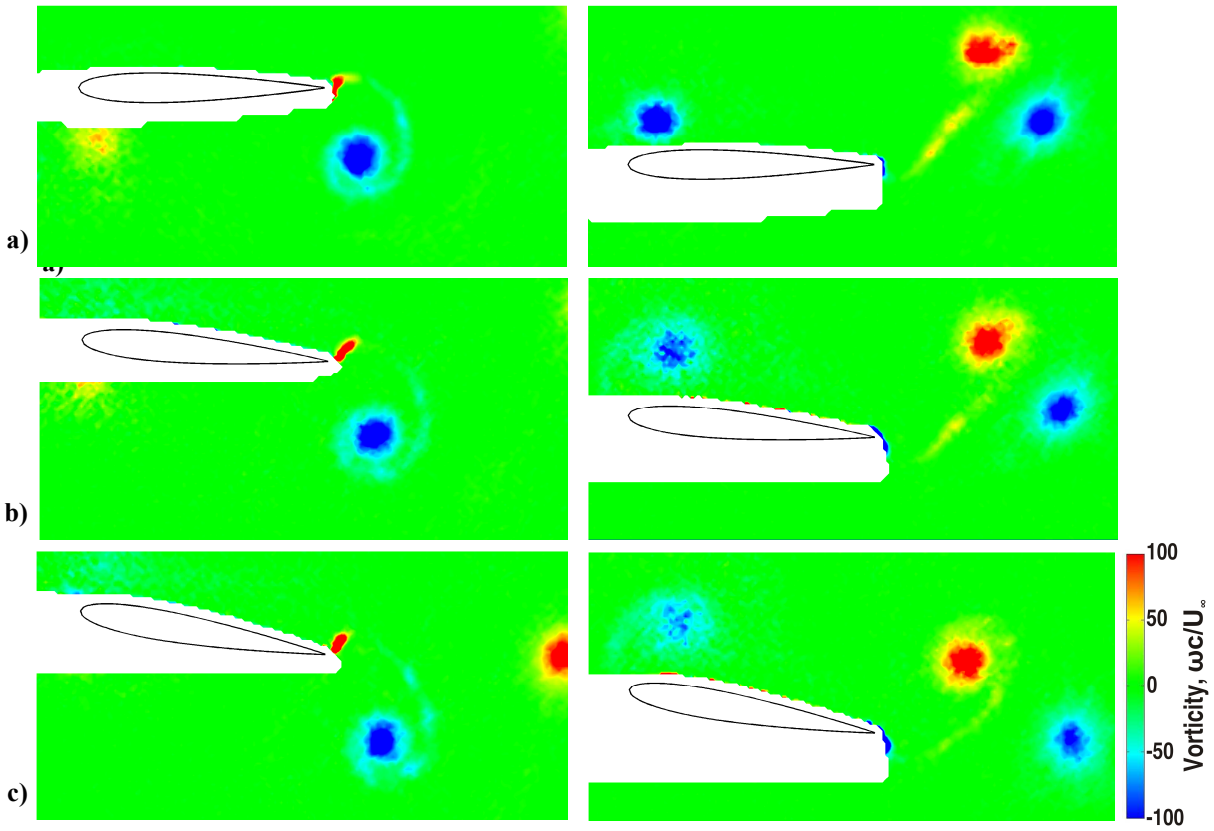

FIGURE 7. Phase-averaged vorticity contour plots at the top (left) and bottom (right) of the motion comparing the mode A flowfield for a/c = 0.15, St_c = 2.025 and: a) α = 0°, b) α = 5°, and c) α = 10°.

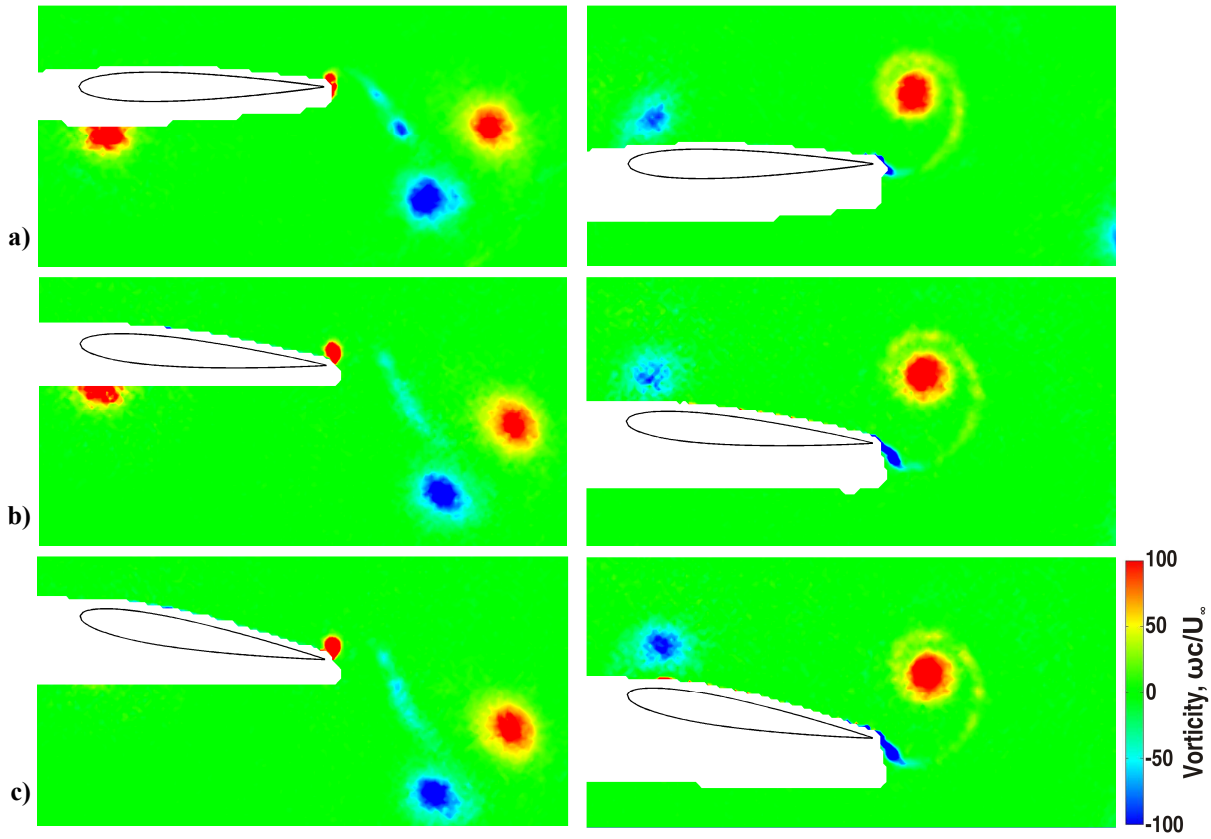

FIGURE 8. Phase-averaged vorticity contour plots at the top (left) and bottom (right) of the motion comparing the mode B flowfield for a/c = 0.15, St_c = 2.025 and: a) α = 0°, b) α = 5°, and c) α = 10°

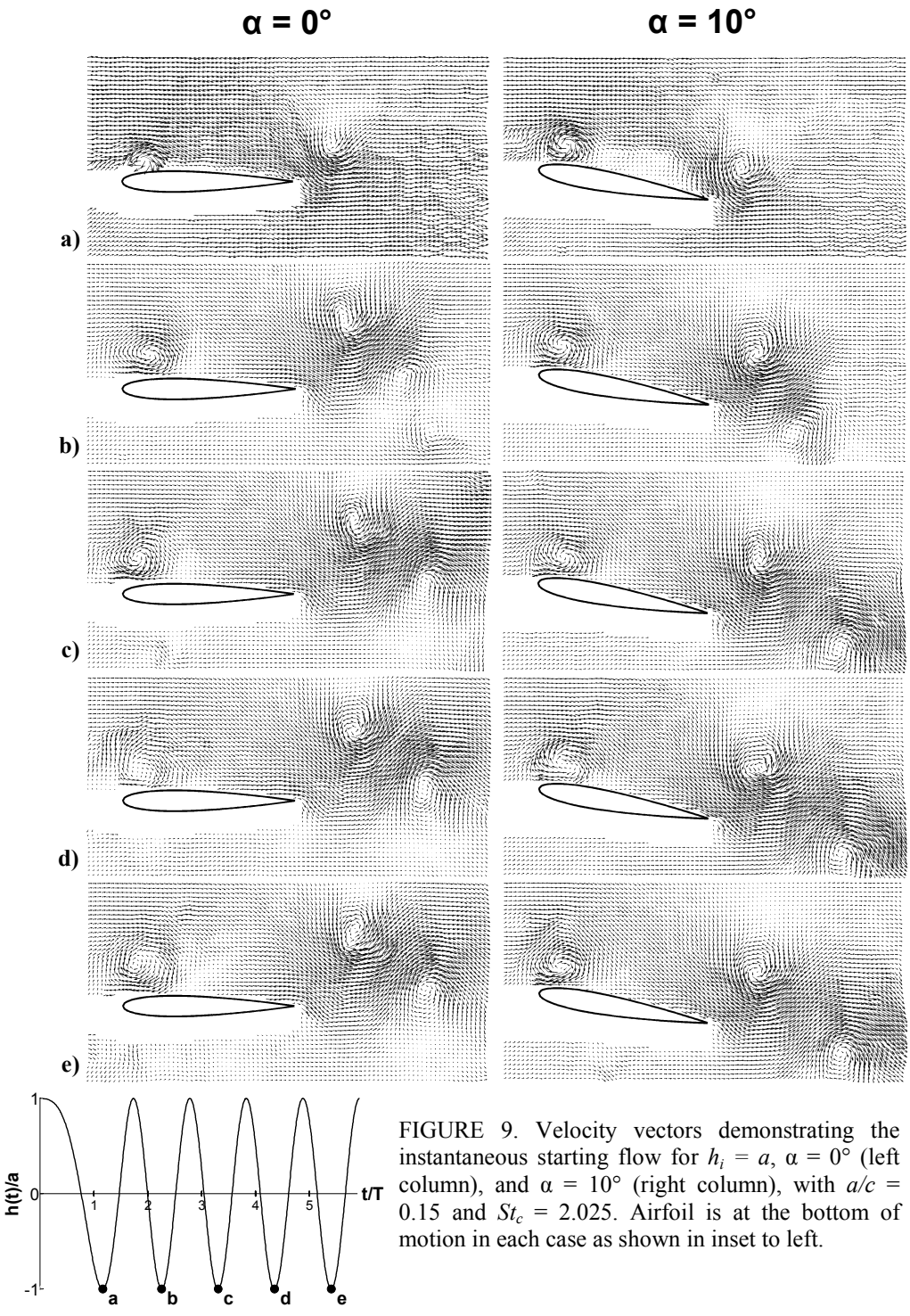

FIGURE 9. Velocity vectors demonstrating the instantaneous starting flow for $h_i = a$, α = 0° (left column), and α = 10° (right column), with a/c = 0.15 and St_c = 2.025. Airfoil is at the bottom of motion in each case as shown in inset to left.

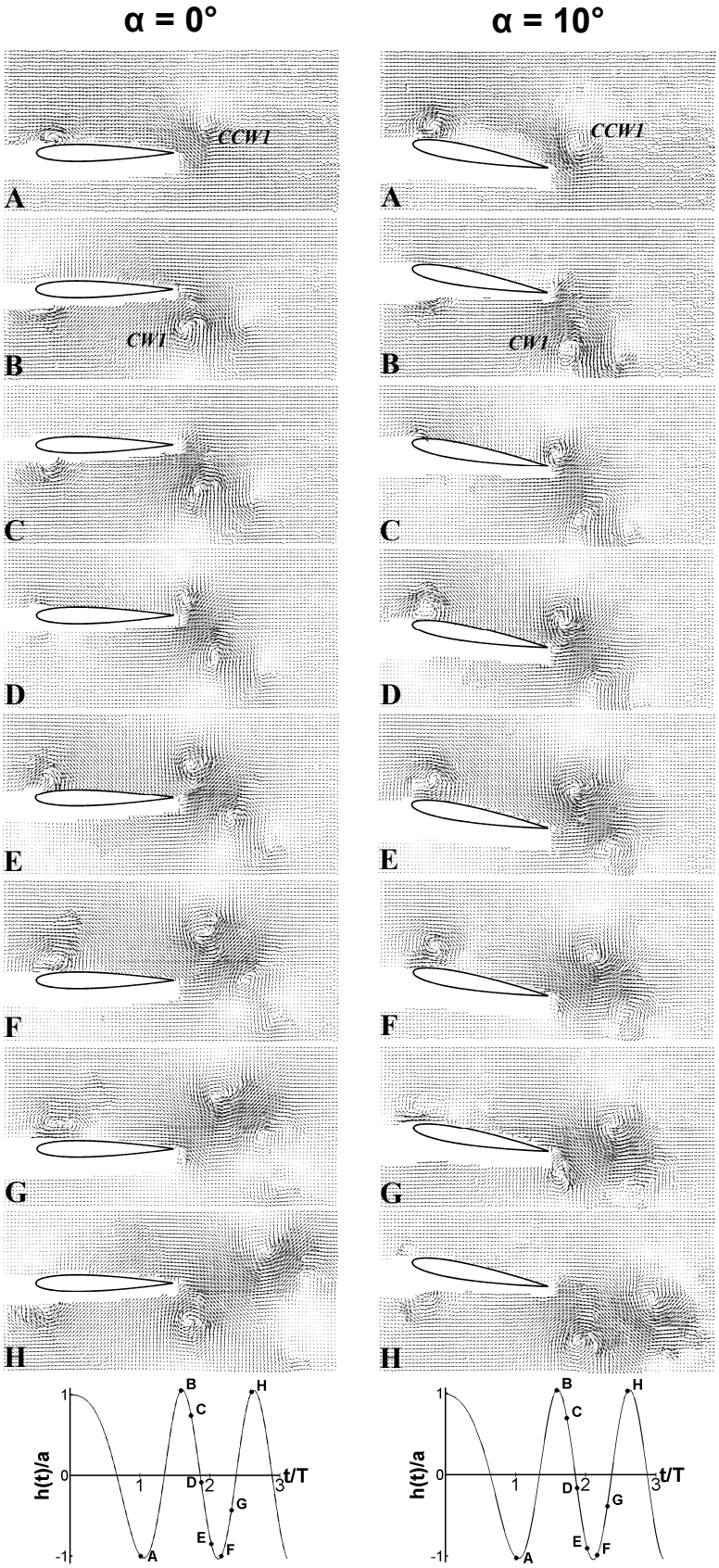

FIGURE 10. Velocity vectors demonstrating the instantaneous starting flow for a/c = 0.15 and St_c = 2.025, h_i = a, α = 0° (left column), and α = 10° (right column). Note the stronger first counter-clockwise vortex (CCW1) in the α = 10° case. This pairs with the first clockwise vortex, drawing it downwards and thereby creating a downward deflected jet.

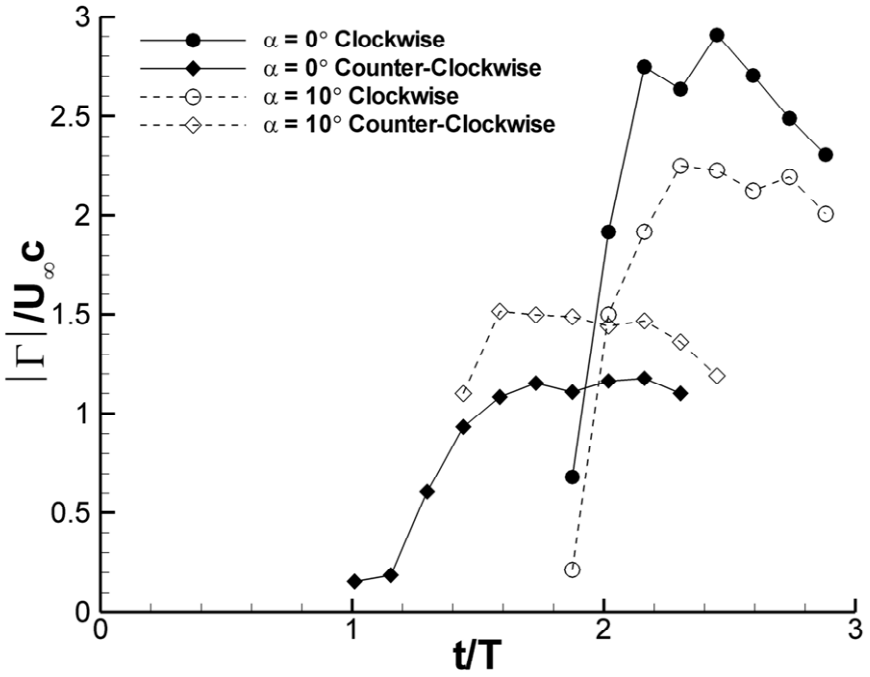

FIGURE 11. Normalized circulation of the first two trailing edge vortices formed during the starting process from $h_i = a$, for α = 0° and α = 10°.

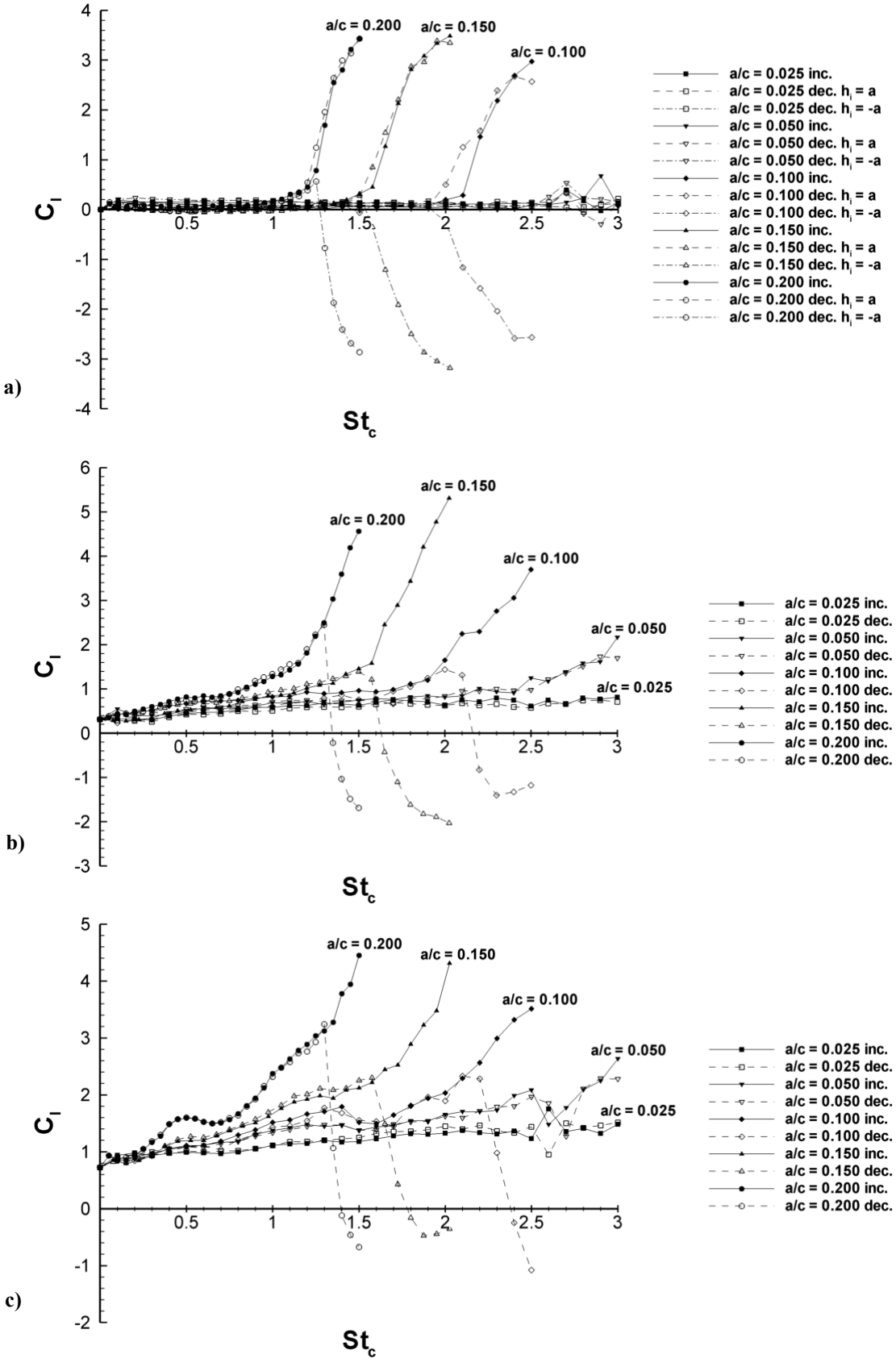

FIGURE 12. Lift coefficient as a function of St_c for: a) α = 0°, b) α = 5°, c) α = 10°, and d) α = 15°. Increasing frequency: solid lines and full symbols; decreasing frequency: dashed lines and open symbols. Unless stated in the legend the starting position for decreasing frequency is $h_i = 0$ ($(t/T)_s = 0.25$). Continued on next page.

d)

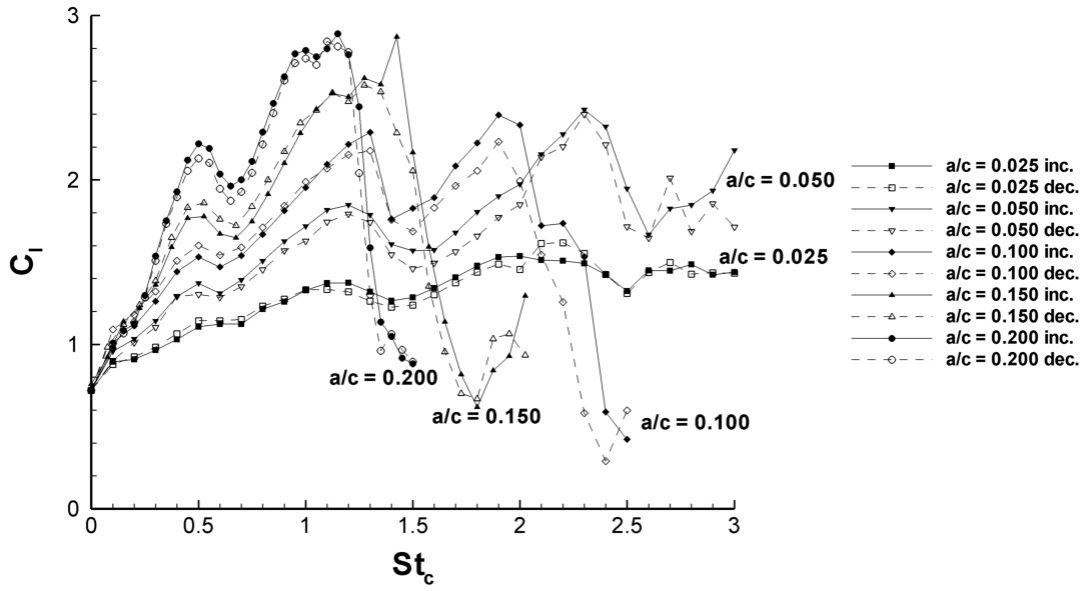

FIGURE 12. Continued

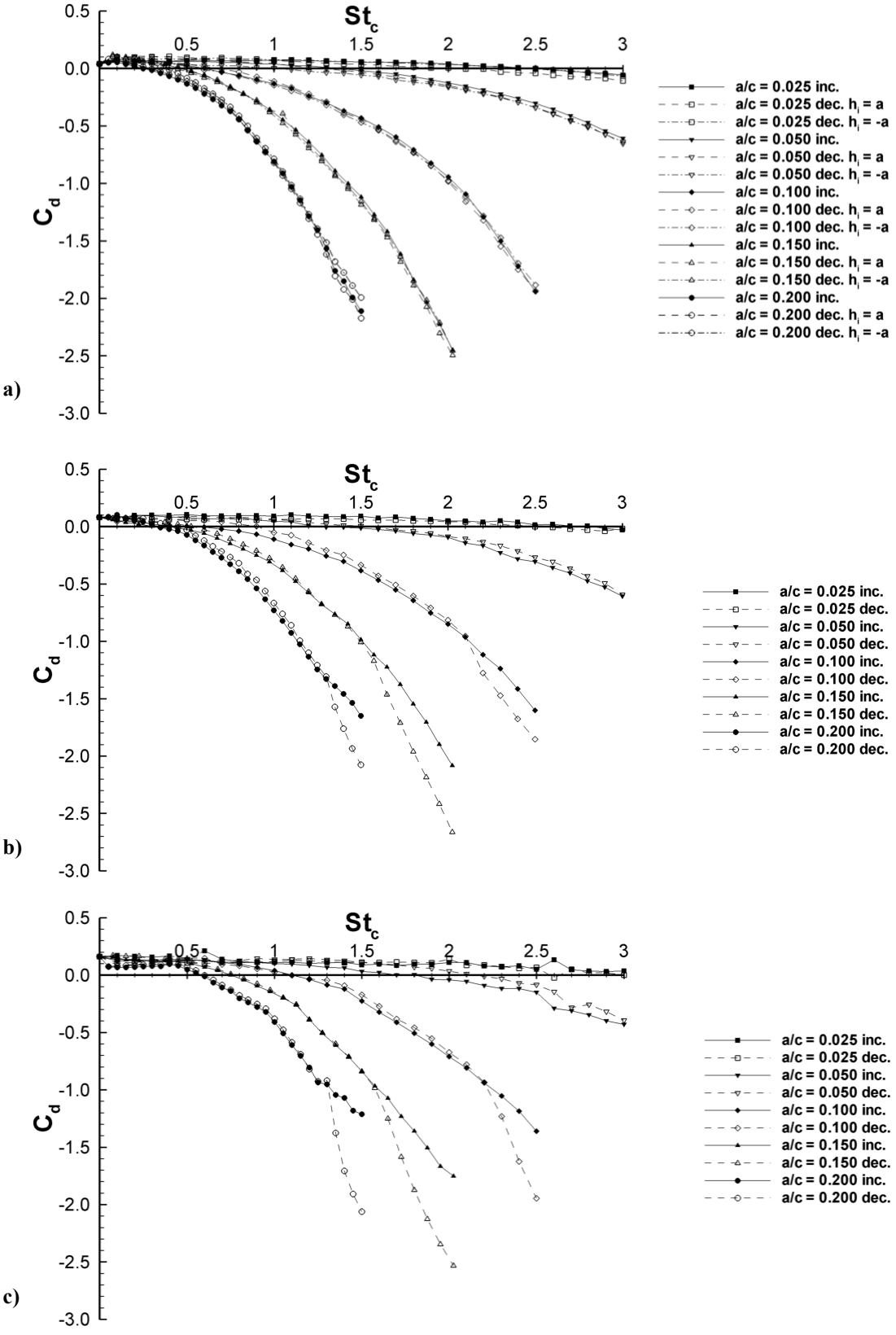

FIGURE 13. Drag coefficient as a function of St_c for: a) α = 0°, b) α = 5°, c) α = 10°, and d) α = 15°. Increasing frequency: solid lines and full symbols; decreasing frequency: dashed lines and open symbols. Unless stated in the legend the starting position for decreasing frequency is $h_i = 0$ ($(t/T)_s = 0.25$). Continued next page.

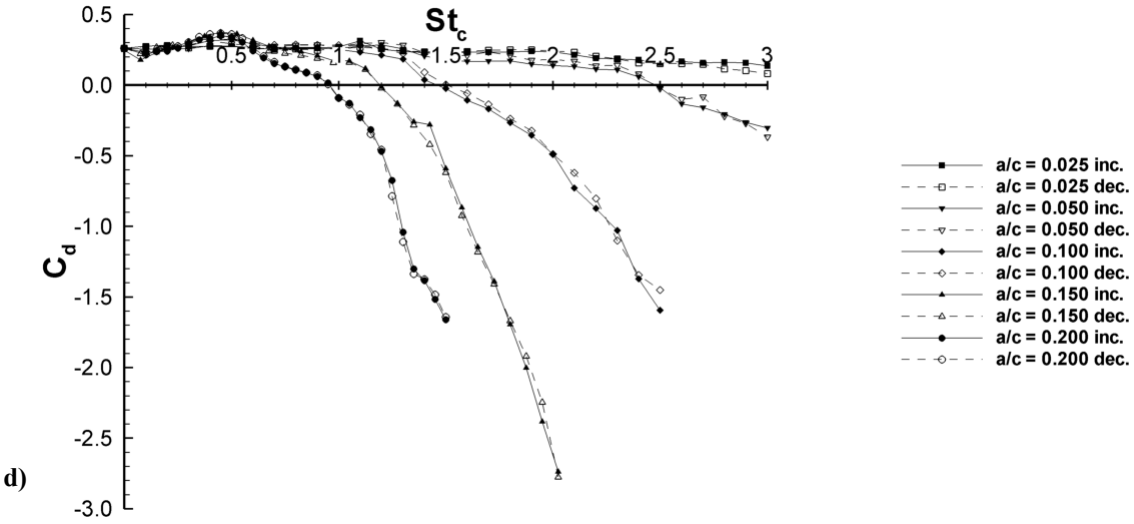

d)

FIGURE 13. Continued

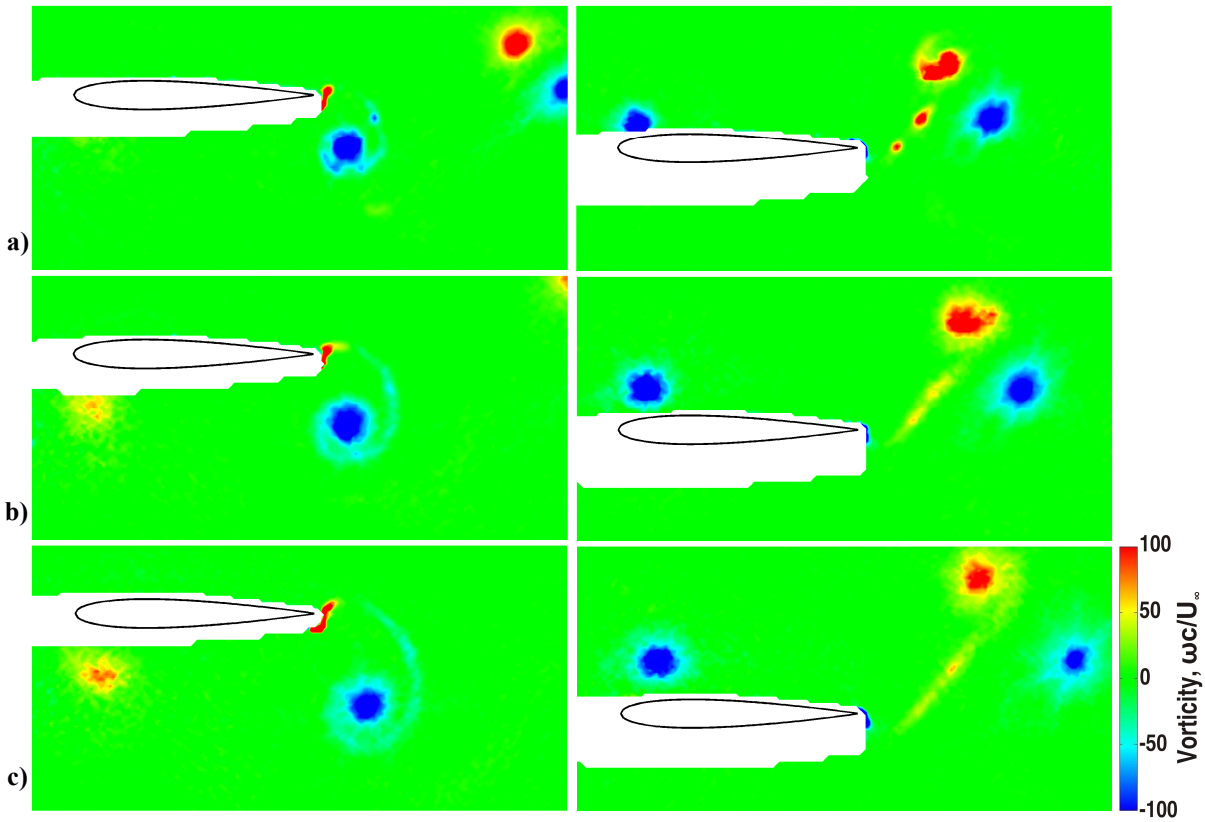

FIGURE 14. Phase-averaged vorticity contour plots at the top (left) and bottom (right) of the motion comparıng the mode A flowfield for α = 0°, and: a) a/c = 0.10, St_c = 2.500, b) a/c = 0.15, St_c = 2.025, and c) a/c = 0.20, St_c = 1.500.

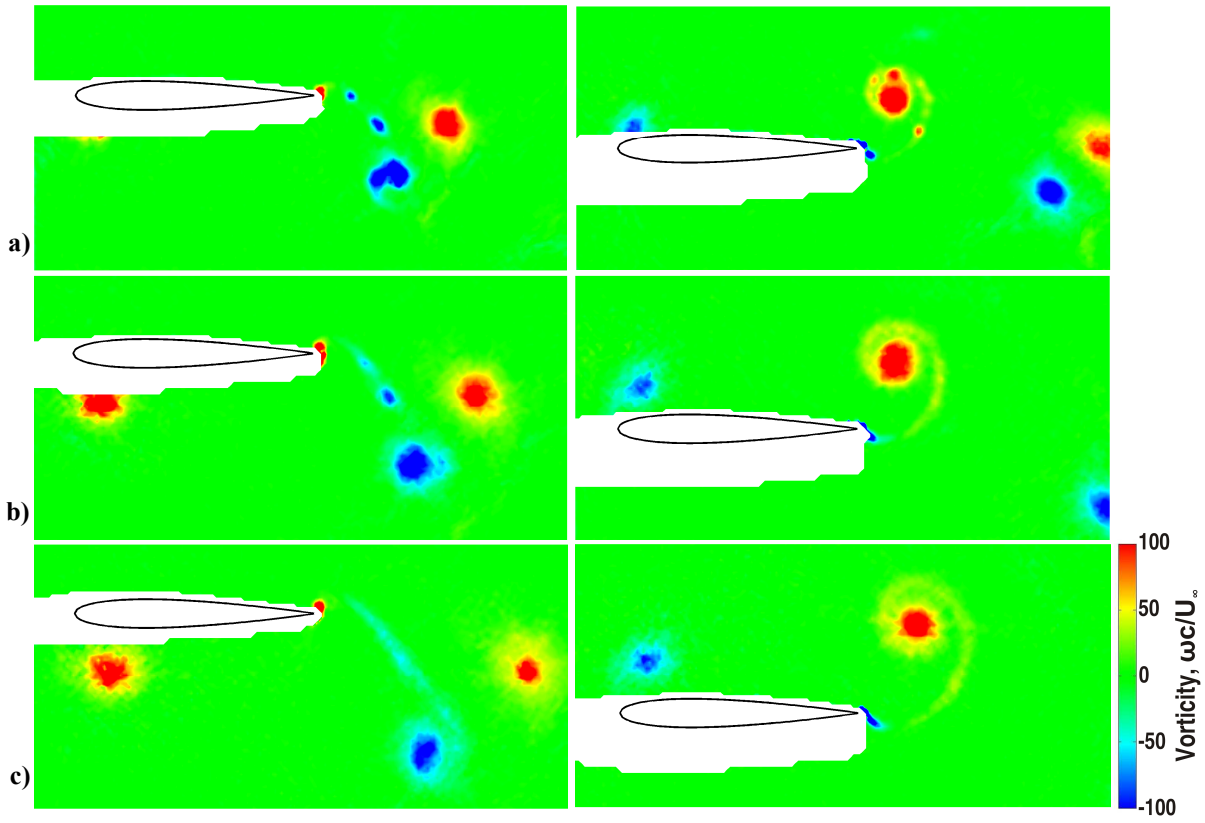

FIGURE 15. Phase-averaged vorticity contour plots at the top (left) and bottom (right) of the motion comparing the mode B flowfield for α = 0°, and: a) a/c = 0.10, St_c = 2.500, b) a/c = 0.15, St_c = 2.025, and c) a/c = 0.20, St_c = 1.500.

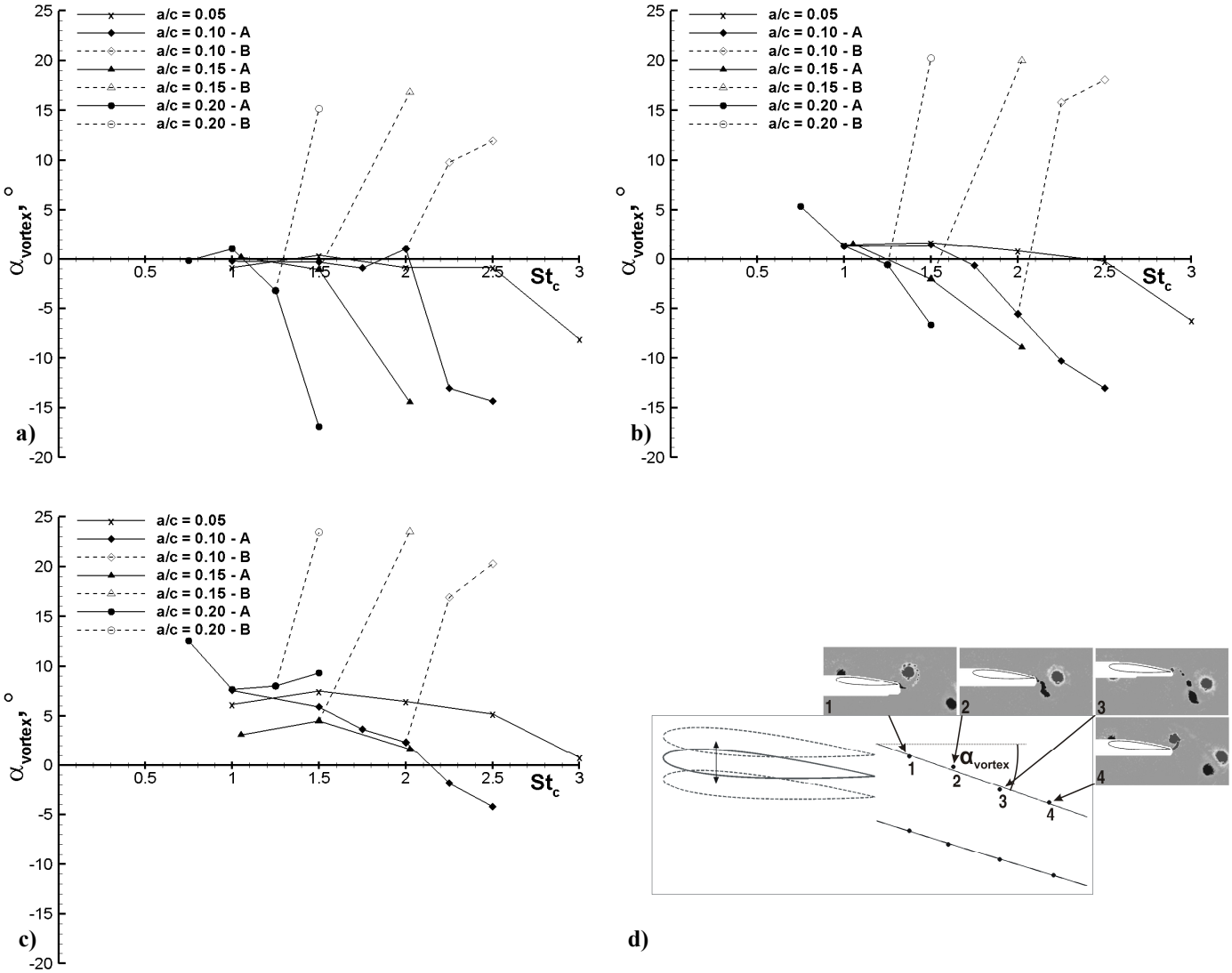

FIGURE 16. Trailing edge vortex trajectory angle for: a) α = 0°, b) α = 5°, and c) α = 10°; and d) method used to determine α_{vortex} for the counter-clockwise TEV. It is first located in the phase-averaged data, a line of best fit is then applied giving a gradient related to α_{vortex}. The sign convention for α_{vortex} is positive for a downwards deflected jet, and negative for an upwards deflected jet.

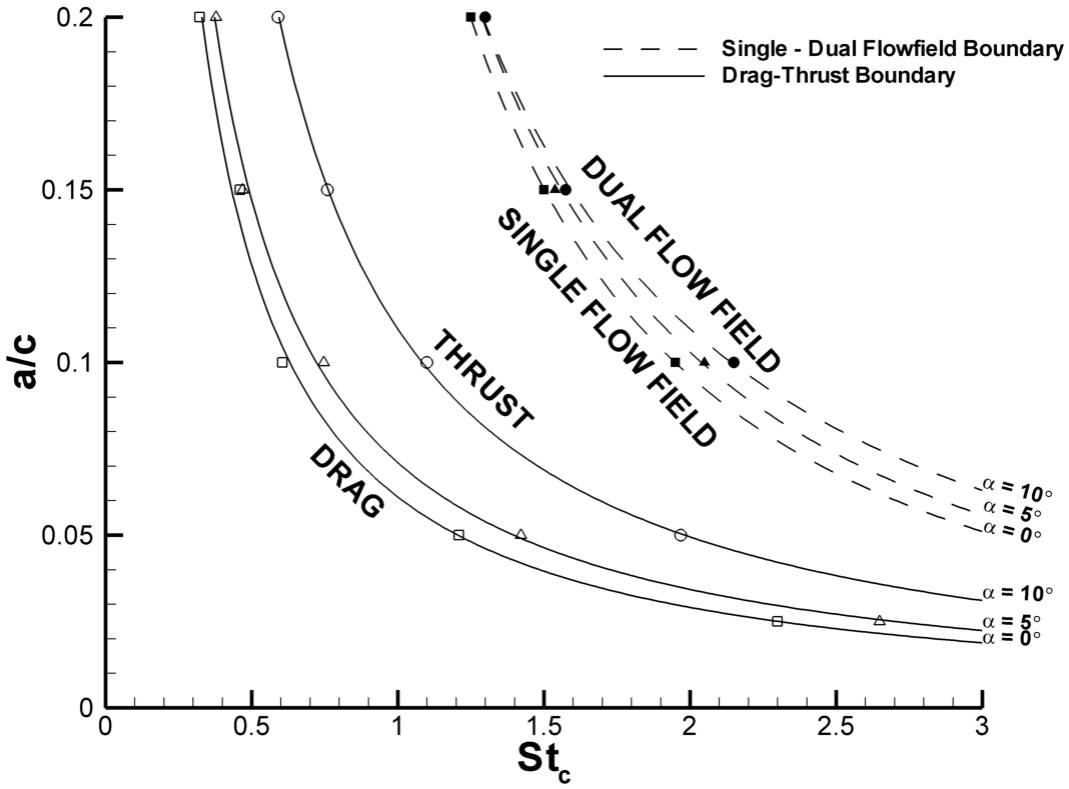

FIGURE 17. Boundary between drag / thrust producing and single / dual flowfield for: α = 0° (square), α = 5° (triangle), and α = 10° (circle). Lines are power law curve fits.

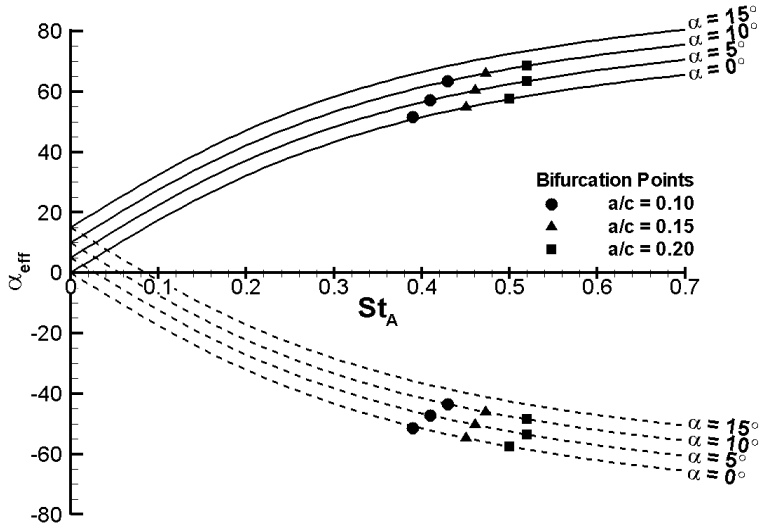

FIGURE 18. Effective angle of attack as a function of Strouhal number based on amplitude. Solid line: $\alpha_{eff,max}$, dashed line: $\alpha_{eff,min}$. Symbols denote the point of bifurcation as determined from the force measurements.

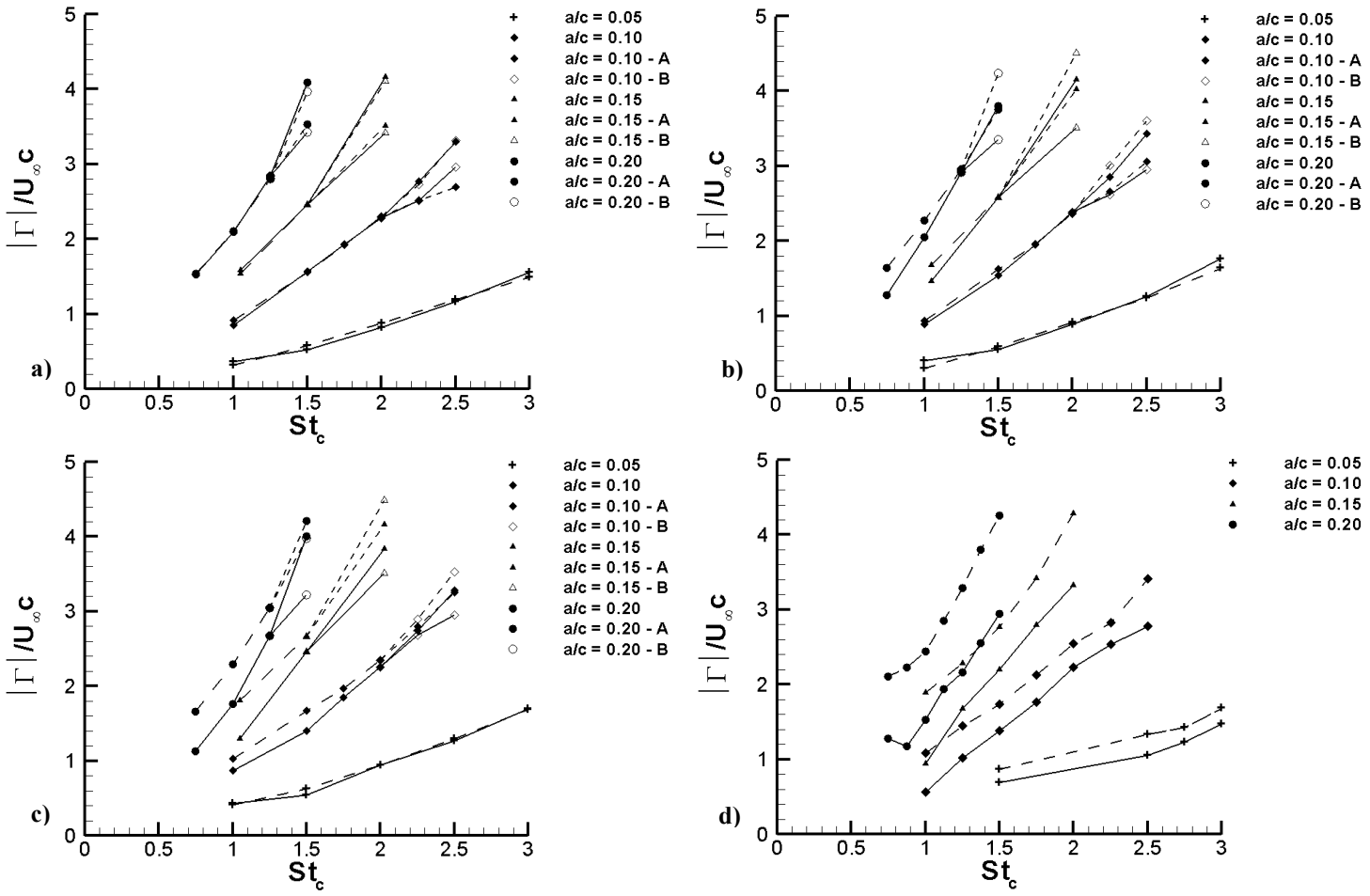

FIGURE 19. Absolute circulation for: a) α = 0°, b) α = 5°, c) α = 10°, and d) α = 15°. Solid line represents the clockwise TEV, and dashed line the counter-clockwise TEV.

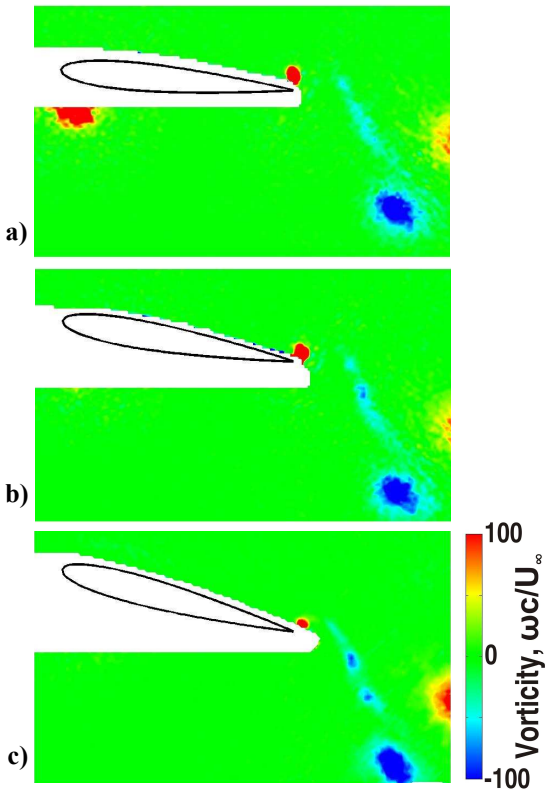

FIGURE 20. Vorticity contours showing the similarity of flowfields across different angles of attack for *a/c* = 0.150, St_c=2.025 and: a) α = 5° - mode B, b) α = 10° - mode B, and c) α = 15°.

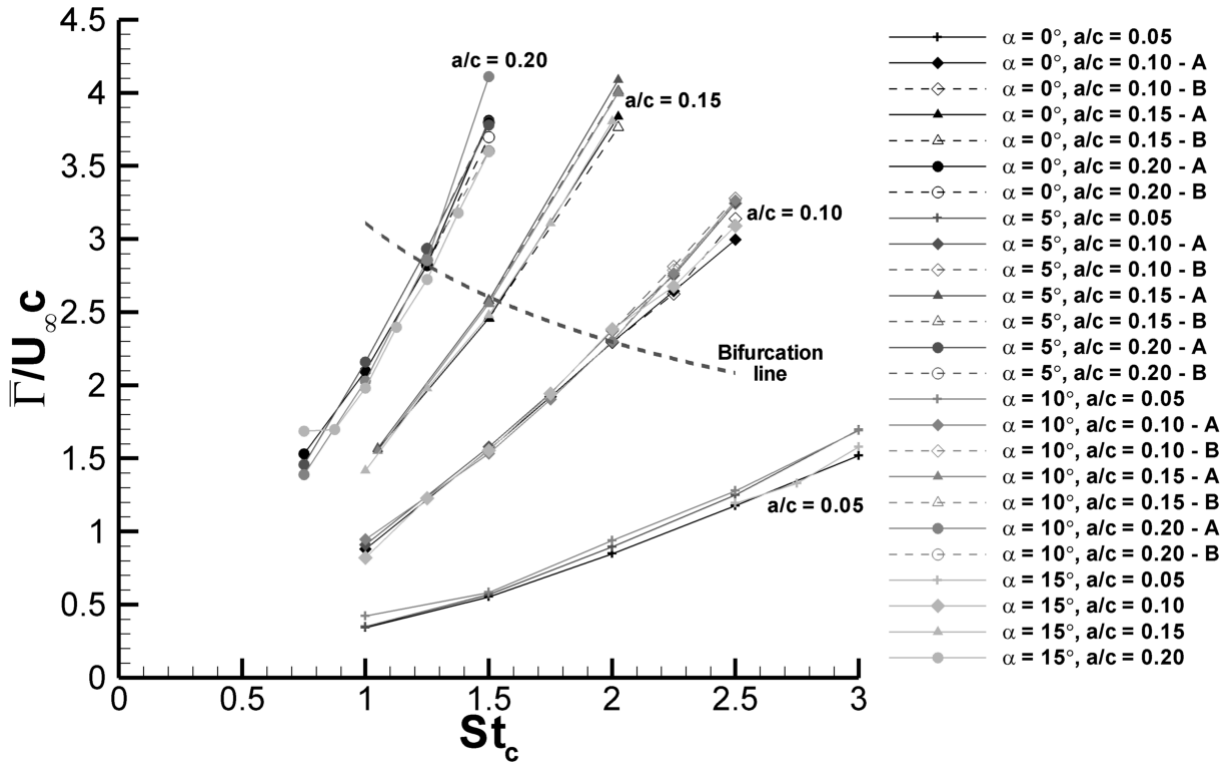

FIGURE 21. Average absolute TEV circulation as a function of Strouhal number.

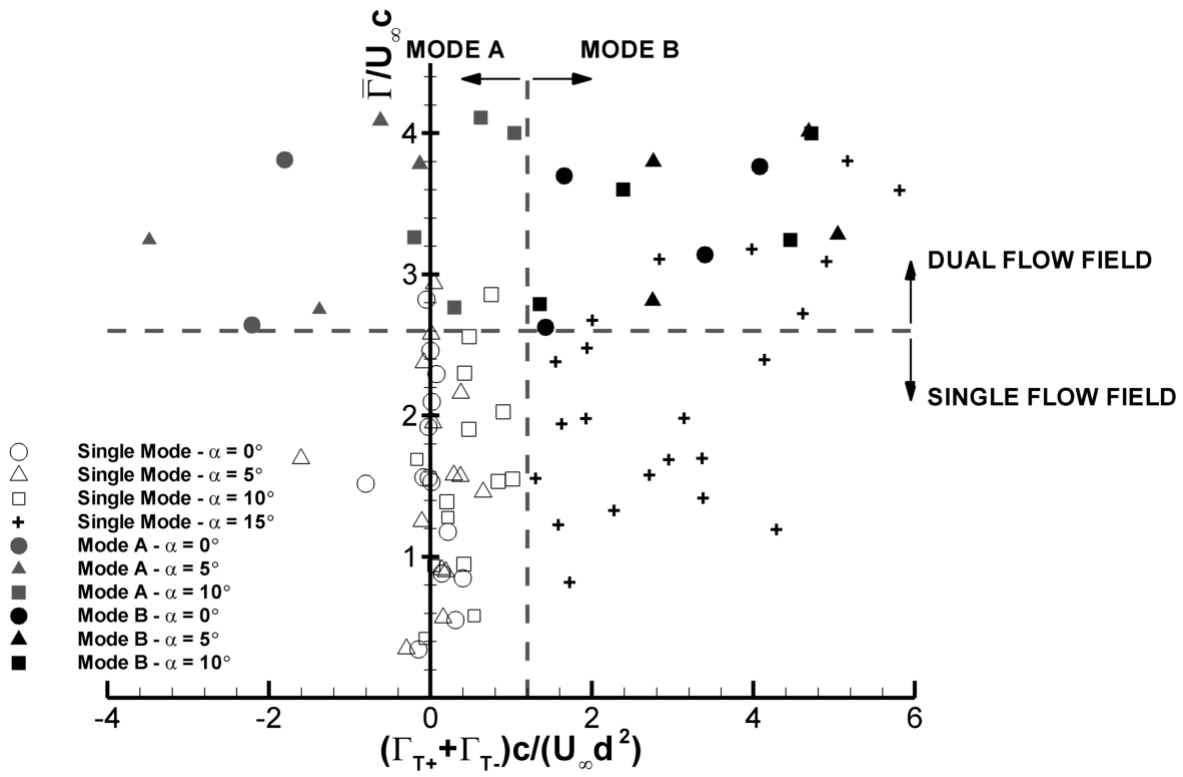

FIGURE 22. Normalized circulation as a function of asymmetry parameter.

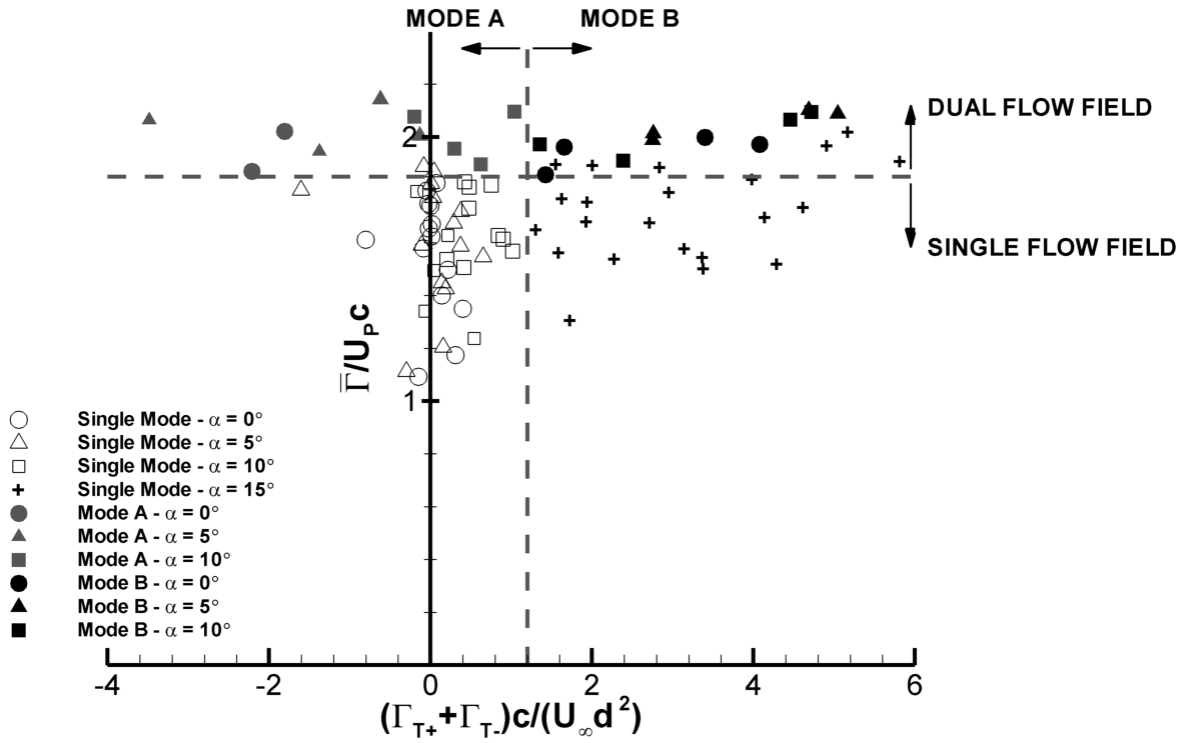

FIGURE 23. Circulation normalized by plunge velocity as a function of asymmetry parameter.

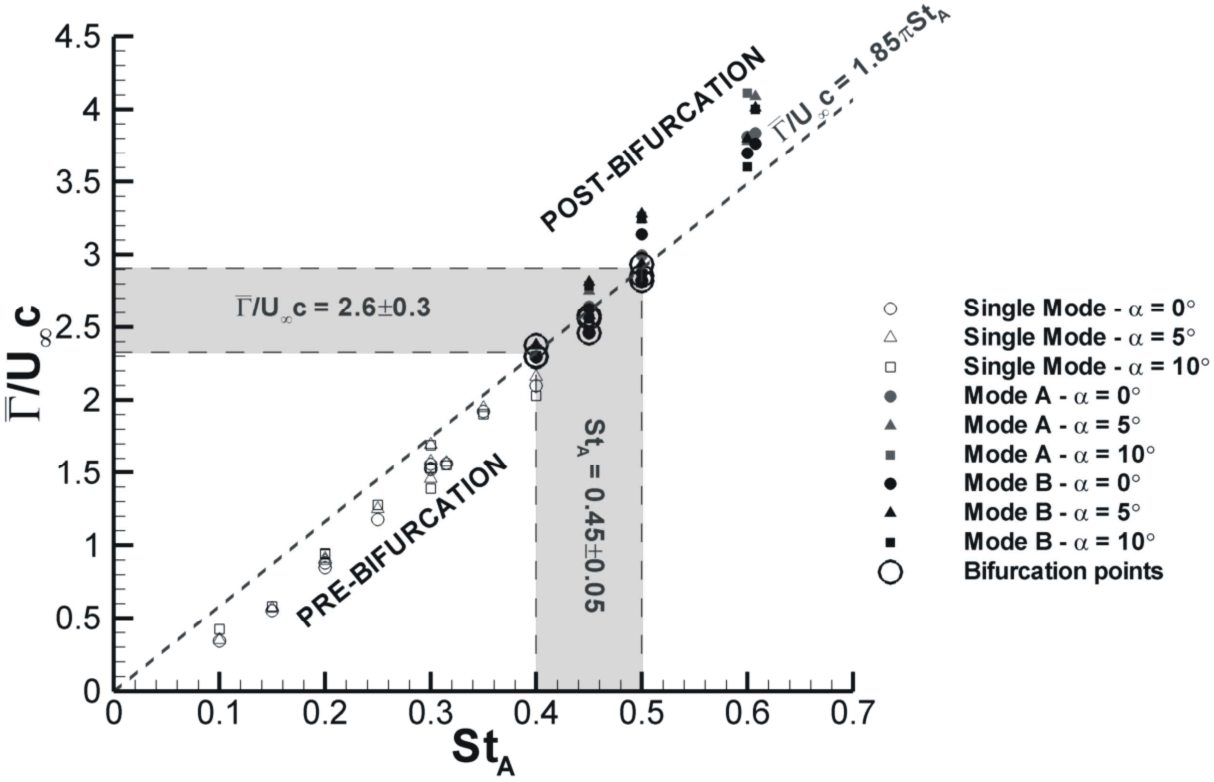

FIGURE 24. TEV normalized circulation as a function of Strouhal number based on amplitude. Large circles highlight the point of bifurcation. Grey dashed line of gradient 1.85π represents the bifurcation constant derived from Figure 23.

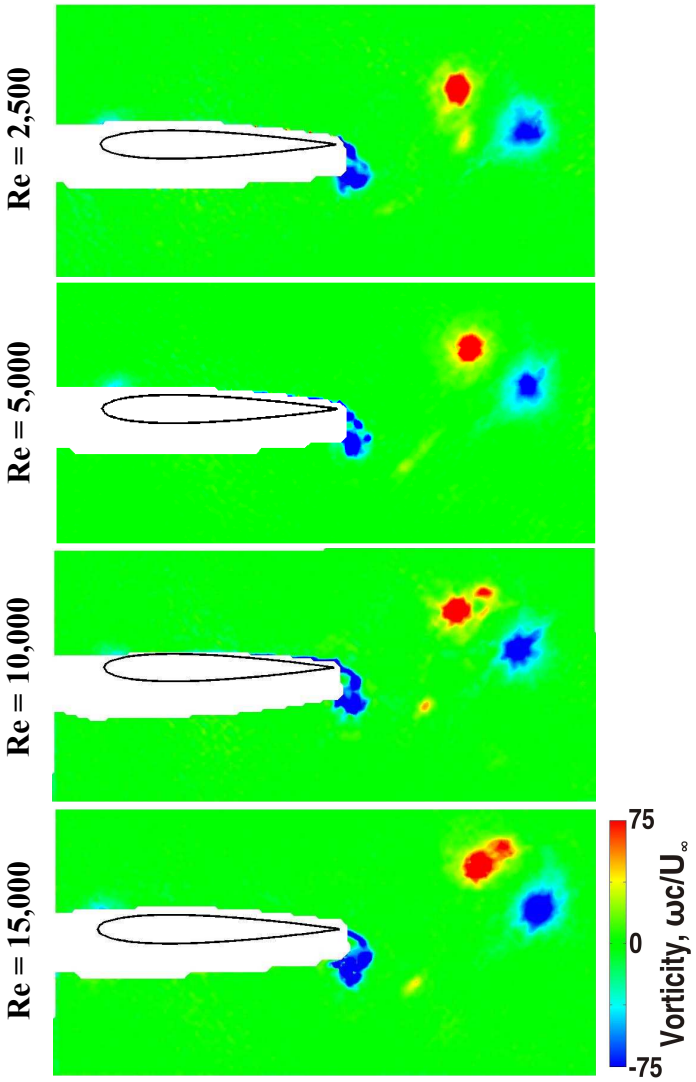

FIGURE 25. Normalized vorticity for different Reynolds numbers, with α = 0°, *a/c* = 0.15, and St_c = 2.25 for *Re* = 2,500; St_c = 2.00 for *Re* = 5,000; St_c = 2.25 for *Re* = 10,000; St_c = 2.25 for *Re* = 15,000.